AN ABSTRACT OF THE THESIS OF

Mark F. Strohecker for the degree of Master of Science in Nuclear Engineering presented on April 21, 1998. Title: Investigation of the IRWST Flow Patterns During a Simulated Station Blackout Experiment on the OSU APEX Facility.

Abstract approved: _____

Todd S. Palmer

The OSU/APEX thermal hydraulic test facility models the passive safety systems of the Westinghouse AP600 advanced light water reactor design. Numerous experiments have been performed to test these systems, the one of focus here is the station blackout scenario. This experiment simulated the complete loss of AC power to all plant systems. One of the objectives of this experiment was to determine the effectiveness of the Passive Residual Heat Removal (PRHR) system. The PRHR system removes heat by rejecting it into the In-containment Refueling Water Storage Tank (IRWST).

The IRWST houses the PRHR and is used as a heat sink for the decay heat. The PRHR is a C-type tube heat exchanger. Heat is removed through two mechanisms: natural convection and nucleate boiling from the surface of the PRHR. As the experiment progressed, a large degree of thermal stratification was observed in the IRWST with no significant thermal mixing. A thermal layer developed in the top of the tank and as the thermal layer approached saturation the rate of heat removal from the sections of the PRHR engulfed by this layer decreased. The effectiveness of these sections of the PRHR

continued to decrease until unexpected flow patterns developed at the same time that the thermal layer reached saturation. The IRWST fluid exhibited a bulk azimuthal flow pattern that increased the effectiveness of the PRHR. This increase allowed for more heat to be injected into the IRWST. However, the bulk fluid motion still did not mix the thermal layers.

A three-dimensional computational fluid dynamic model using the CFX-4.2 software was developed to study the PRHR/IRWST system. The model uses the RPI method to account for the sub-cooled boiling that is present on the PRHR surface. The model successfully predicted the thermal stratification in the IRWST to within 4 K of experimental data. A counter-current flow was shown to occur along the interface of the thermal layers. This caused an enhancement of the heat transfer and turbulent mixing occurring across the interface of the thermal layers.

Investigation of the IRWST Flow Patterns During a Simulated Station Blackout Experiment on the OSU APEX Facility

by

Mark F. Strohecker

A THESIS

submitted to

Oregon State University

in partial fulfillment of
the requirements for the
degree of

Master of Science

Presented April 21, 1998
Commencement June 1998

Master of Science thesis of Mark F. Strohecker presented on April 21, 1998

APPROVED:

Major Professor, representing Nuclear Engineering

Chair of Department, of Nuclear Engineering

Dean of the Graduate School

I understand that my thesis will become part of the permanent collection of Oregon State University libraries. My signature below authorizes release of my thesis to any reader upon request.

Redacted for privacy

Mark F. Strohecker, Author

Acknowledgments

First, I would like to thank my parents for not complaining too much when I decided to go to school so far away from home. I would also like to thank my sister for always arranging my plane tickets to come home, without her I would be stranded in Oregon for the rest of my life. Yes, I am truly that helpless.

The one person who deserves a great deal of credit is Dr. Todd Palmer. I could thank you for many things but the one thing that I am most thankful for is your patience. Most professors would not have put up with my ranting and raving as much as you have. For that I am thankful.

Dr. Jose' N. Reyes was also instrumental in the completion of this research. I would like to thank you for the excellent project and the opportunity to work with the APEX facility an staff. This work has opened a lot doors for me.

I would like to thank John Groome, Teresa Culver, and the entire APEX staff for all the help they have been. Their ability to run the APEX project with a high degree of efficiency and order has made my work easier.

Finally, I would like to thank CHADWICK for not complaining about the seemingly endless running. She was the backbone that allowed the completion of this project possible.

Table of Contents

Page

1. Introduction 1

2. Literature Review 3

    2.1 Sub-cooled Boiling Models 4

        2.1.1 RPI model 5
        2.1.2 TRAC/RELAP Model 12

    2.2 Two-Phase Turbulence Effects 15

3. APEX Test Facility Description 19

    3.1 Primary System 19

    3.2 Passive Safety System 20

    3.3 Break and ADS Measurement System (BAMS) 23

    3.4 Instrumentation 24

    3.5 Critical Components and Instrumentation 25

        3.5.1 Passive Residual Heat Removal System 26
        3.5.2 Automatic De-pressurization System Sparger 28
        3.5.3 In-containment Refueling Water Storage Tank 29

4. Description of Experiment 31

    4.1 Test Objective 31

    4.2 Test Description 32

        4.2.1 Secondary Side Blowdown Phase 32
        4.2.2 Natural Circulation Phase 33
        4.2.3 ADS Operation Phase 36
        4.2.4 IRWST Injection Phase 37
        4.2.5 Sump Recirculation Phase 37

    4.3 Test Observations 37

Table of Contents (Continued)

Page

4.4 Further Study 40

5. CFX-4.2 Description 41

5.1 Geometry and Grid Generation 41

5.2 Flow Solver Options 46

5.2.1 Transport Equations 47

5.2.1.1 Single-Phase Equations 47
5.2.1.2 Multi-Phase Equations 49

5.2.2 Turbulence Models 51

5.2.2.1 Reynolds Averaged Equations 51
5.2.2.2 Eddy Viscosity Models 53
5.2.2.3 Second Order Closure Models 55
5.2.2.4 Multi-Phase Turbulent Flows 56

5.2.3 Multi-Phase Interfacial Relations 58

5.2.3.1 Inter-Phase Drag 58
5.2.3.2 Non-Drag Forces 60
5.2.3.3 Inter-Phase Heat Transfer 60
5.2.3.4 Inter-Phase Mass Transfer 61

5.2.4 Numerical Algorithm 61

5.3 Graphical Visualization 64

6. IRWST/PRHR Model 65

6.1 Preliminary Model 65

6.1.1 Geometry and Grid 66
6.1.2 Flow Model 68
6.1.3 Result and Discussion of the Preliminary Model 70

6.2 Final Model 73

Table of Contents (Continued)

Page

6.2.1 Geometry and Grid 73
6.2.2 Flow Model 77
6.2.3 Results and Discussion 79

6.2.3.1 Thermal Stratification 80
6.2.3.2 IRWST Hydrodynamics 85
6.2.3.3 Counter-Current Flow 90
6.2.3.4 Void Distribution 93
6.2.3.5 PRHR Between Flow 95

6.3 Sources of Error 97

6.3.1 Numerical Errors 97
6.3.2 Geometry Errors 99
6.3.3 Assumptions and Choice of Models 100

7. Conclusions and Future Work 103

Bibliography 107

List of Figures

Figure Page

3.1 The APEX Test Facility 22

3.2 Schematic of APEX System 22

3.3 PRHR Heat Exchanger 26

3.4 PRHR System Flow 27

3.5 PRHR Instruments 28

3.6 IRWST Instrumentation 30

4.1 IRWST Fluid Temperature History 34

4.2 Heat Removal from the PRHR 35

4.3 Map of the PRHR Heat Exchanger Zones 35

4.4 PRHR Zonal Heat Rejection Fractions 36

5.1 Single/Multi-Block Topology Comparison 43

5.2 Single/Multi-Block Grid Comparison 44

5.3 Computational Flow-chart 63

6.1 Block Network of Preliminary IRWST Model 67

6.2 Grid for the Preliminary IRWST Model 68

6.3 Temperature (Kelvin) in the IRWST 70

6.4 Velocity (m/s) of the IRWST Fluid at Different Times 71

6.5 U-Velocity (m/s) at the Mid-plane between the IRWST and the PRHR 72

6.6 Block Network of the Final Model 74

6.7 Grid for the Final IRWST Model 74

List of Figures (continued)

Figure Page

6.8 Block Network of the PRHR 75

6.9 PRHR Grid 76

6.10 Thermal Stratification (Kelvin) in the IRWST 81

6.11 Thermal Stratification (Kelvin) in the IRWST (continued) 82

6.12 Comparison between CFX and Experimental Data for Thermocouple TF-709 83

6.13 Comparison between CFX and Experimental Data for Thermocouple TF-708 84

6.14 Comparison between CFX and Experimental Data for Thermocouple TF-707 84

6.15 U-Velocity (m/s) above the IRWST at 3,000 seconds 85

6.16 U-Velocity (m/s) above the IRWST at 8,000 seconds 86

6.17 W-Velocity (m/s) between the PRHR 87

6.18 W-Velocity (m/s) between the PRHR (continued) 88

6.19 Overall Speed (m/s) of the IRWST Water at 8,000 seconds 89

6.20 U-Velocity (m/s) between the PRHR 91

6.21 V-Velocity (m/s) around the PRHR 92

6.22 Void Fraction around Zone 1 of the PRHR with 5 K of sub-cooling 93

6.23 Void Fraction around the PRHR with 5 K sub-cooling 94

6.24 Void Fraction around Zone 2 of the PRHR with 5 K sub-cooling 94

6.25 Liquid W-Velocity (m/s) Through the PRHR 96

6.26 Vapor W-Velocity (m/s) Through the PRHR 96

6.27 Energy Control Volume 101

Investigation of the IRWST Flow Patterns During a Simulated Station Blackout Experiment on the OSU APEX Facility

Chapter 1. Introduction

This document presents a study of the flow patterns within the In-containment Refueling Water Storage Tank (IRWST) of the OSU APEX thermal-hydraulic test facility and the implications on the Passive Residual Heat Removal (PRHR) system. The APEX facility is a one-quarter scaled version of the Westinghouse advanced light water reactor design, the AP600. The APEX is designed to test the passive safety systems of the Westinghouse design.

These flow patterns were found to be most prevalent in the station blackout experiment, NRC-5102. This experiment simulates the complete loss of power to all plant systems. This loss of power causes the reactor coolant pumps to trip and the safety systems to initiate. The control rods are immediately inserted to shutdown the power generation by the reactor core. However, the decay heat still needs to be removed from the core and this is accomplished with the PRHR heat exchanger. The PRHR is a C-type tube heat exchanger.

The IRWST houses the PRHR and is used as a heat sink for the decay heat. The IRWST is initially filled with stagnant, sub-cooled water at atmospheric pressure. Heat is removed through natural convection and nucleate boiling from the surface of the PRHR. As the experiment progressed, a large degree of thermal stratification was observed in the IRWST. A saturated layer developed in the top of the tank and slowly extended down

into the bottom half of the IRWST. The stratified layers did not significantly mix during the experiment and as this layer grew the rate of heat removal from the sections of the PRHR engulfed by the saturated layer decreased. The effectiveness of the covered sections of the PRHR continued to decrease until an unexpected flow pattern developed. The IRWST fluid exhibited a bulk azimuthal flow pattern that increased the effectiveness of the PRHR. This increase allows for more heat to be injected into the IRWST. However, the bulk fluid motion still did not mix the thermal layers.

The objectives of this research are two-fold. The first objective is to study the effect that the thermal stratification and the flow patterns in the IRWST have on the heat removal from the PRHR. The study was performed by using a commercial computational fluid dynamics (CFD) software package, CFX4.2. CFX4.2 was used to generate the geometry and the grid of the IRWST/PRHR system and to solve the multi-fluid transport equations with a mechanistic sub-cooled boiling model.

The second objective is to determine the usefulness of such CFD packages for nuclear applications. The study will show how accurately CFD can simulate experiments that involve complex phenomena such as: disperse turbulent two-phase flows, and boiling/condensation mechanisms. The reliability of these codes in describing the complex geometries that are generally found in power plant systems was also studied. The most important question that needs to be answered is can CFD codes predict realistic behaviors for the AP600. Confidence in there ability to do so is gained by comparisons with scaled experiments such as the APEX facility.

Chapter 2. Literature Review

The number of necessary simplifications of the multi-fluid transport equations derived by Ishii [1], for example, has been drastically reduced in recent years with the advent of the high CPU speeds exhibited by the modern computer. These simplifications have brought about numerous models that offer a great deal of insight into two-phase systems. Two of the most popular are the homogenous equilibrium model (HEM) and the drift flux model. The homogenous equilibrium model assumes that the phases are in thermal, mechanical and chemical equilibrium. This means that both phases share the same velocity, temperature and pressure field. Therefore the system can be represented as a mixture and the two-fluid equations simplify into a pseudo single phase calculation. HEM is adequate for solving problems at high pressure and high flow rate conditions. It can also be used in drag dominated flows, since the phasic velocity fields tend to equalize over short distances.

The drift flux model is similar to the homogenous model. It only differs in that it allows the phasic velocities to differ. The phasic velocities are related to each other by a predetermined algebraic equation. The drift flux model yields accurate solutions for low pressure and/or low flow rate systems.

The non-equilibrium nature of sub-cooled nucleate boiling does not permit the use of the previously described models, at least not in good conscience. Instead the multi-fluid model has been used for this task in numerous situations. The multi-fluid model allows for the proper prediction of the flow fields for two-phase systems. Two sets of equations are solved, one for each phase, and the information is shared between

the two sets of equations by the interfacial transport of mass, momentum and energy. These multi-fluid equations are being used more often since they can now be solved numerically with relative ease and with few simplifying assumptions. The multi-fluid model is employed in several nuclear safety codes such as TRAC and RELAP, as well as in general CFD packages such as CFX, FLUENT and PHEONICS.

Numerous models have been developed in the area of sub-cooled nucleate boiling. Two possible approaches are taken in the development of these models. One is a mechanistic approach, which consists of a predictive model that includes a closed set of field, state and constitutive equations. These equations are developed by examining the underlying mechanisms which cause the particular phenomena of interest. The other approach is a non-mechanistic model. A non-mechanistic model is based solely on the macroscopically observed properties of phase change, i.e. a simple thermodynamic relation involving the latent heat.

2.1 Sub-cooled Boiling Models

A variety of work has been done in the development of mechanistic models for sub-cooled boiling. The latest and possibly the most complete model is the RPI (Rensselaer Polytechnic Institute) model developed by Kurul [2]. Prior to the RPI model, the models employed by the TRAC [3] and RELAP [4] codes were the prevailing models. The TRAC and RELAP models are nearly identical.

2.1.1 RPI Model

The RPI model is unique because it is the only model that includes the multi-dimensional effects of nucleate boiling. The rate of phase change is highly dependent upon the lateral motion of the vapor phase (steam) towards the liquid phase (water). This lateral motion cannot be described mechanistically in one-dimensional models. One dimensional models also cannot properly predict entrance effects in a channel and the effects that fast transients will have on a system.

The RPI model was developed for forced flow in channels. However, as will be evident, the model is easily extended into the area of pool boiling by choosing the constitutive relations appropriately.

The transport equations are written for each phase and are shown in equations (2.1) through (2.3).

$$\frac{\partial}{\partial t}\left(\alpha_k \rho_k\right) + \nabla \bullet \left(\alpha_k \rho_k \boldsymbol{U}_k\right) = \Gamma_k \tag{2.1}$$

$$\begin{aligned}\frac{\partial}{\partial t}\left(\alpha_k \rho_k \boldsymbol{U}_k\right) + \nabla \bullet \left(\alpha_k \rho_k \boldsymbol{U}_k \boldsymbol{U}_k\right) &= \nabla \bullet \left[\alpha_k \mu_k^e \left(\nabla \boldsymbol{U}_k + (\nabla \boldsymbol{U}_k)^T\right)\right] \\ &- \alpha_k \nabla P_k + \alpha_k \rho_k \boldsymbol{g} + \boldsymbol{U}_{ki} \Gamma_k + \boldsymbol{M}_k\end{aligned} \tag{2.2}$$

$$\begin{aligned}\frac{\partial}{\partial t}\left(\alpha_k \rho_k H_k\right) + \nabla \bullet \left(\alpha_k \rho_k \boldsymbol{U}_k H_k - \alpha_k \lambda_k^e \nabla T_k\right) &= \frac{\partial}{\partial t}\left(\alpha_k P_k\right) + Q_k \\ &+ H_{ki} \Gamma_k + E_k\end{aligned} \tag{2.3}$$

The terms α_k, ρ_k, P_k, $\boldsymbol{U}_k$, T_k and H_k are the volume fraction, density, pressure, velocity, temperature and enthalpy of phase 'k', respectively. The terms Γ_k, $\boldsymbol{M}_k$, and E_k are the

interfacial transport terms of mass, momentum and energy, respectively, and μ_k^e and K_k^e are the effective viscosity and effective thermal conductivity of phase 'k', respectively. Q_k is the energy source (or sink) for phase 'k'.

The most important aspect of modeling two-phase flows is to specify the constitutive relation correctly, which includes specifying Γ_k, M_k, E_k, μ_k^e and k_k^e. The closure relations should adhere to several principles. They are:

- A general form of the models should be based on mechanistic considerations, so that non-mechanistic/empirical aspects are limited to only the necessary scalars.
- The models do not violate the fundamental invariance principle. The invariance principle is given by Drew [5] and states that the constitutive models are independent of coordinate systems.
- The models reduce to the known simplified flow conditions.
- For the continuous phase, two-phase flow models reduce to single phase models when the concentration of the dispersed phase approaches zero.

The interfacial momentum relation, $\boldsymbol{M}_k$ (l=liquid; v=vapor), is divided into the following forces: drag, virtual mass, lift, and turbulent dispersion. These forces are shown in equations (2.4) through (2.7).

$$\boldsymbol{M}_l^{drag} = -\boldsymbol{M}_v^{drag} = \frac{1}{2}\rho_l C_D A_i \left(\boldsymbol{U}_v - \boldsymbol{U}_l\right)\left|\boldsymbol{U}_v - \boldsymbol{U}_l\right| \tag{2.4}$$

$$\boldsymbol{M}_l^{vm} = -\boldsymbol{M}_v^{vm} = C_{vm}\alpha_l\rho_l\left(\frac{D\boldsymbol{U}_l}{Dt} - \frac{D\boldsymbol{U}_v}{Dt}\right) \tag{2.5}$$

$$\boldsymbol{M}_l^{lift} = -\boldsymbol{M}_v^{lift} = C_L\rho_l\alpha_l\left(\boldsymbol{U}_v - \boldsymbol{U}_l\right)\times\left|\nabla\times\boldsymbol{U}_l\right| \tag{2.6}$$

$$\boldsymbol{M}_l^{TD} = -\boldsymbol{M}_v^{TD} = C_{TD}\rho_l k_l \nabla\alpha_g \tag{2.7}$$

Additional interfacial forces could be added or subtracted from the problem if appropriate. The C_{vm}, C_L, and C_{TD} terms are given the values of 0.5, 0.5, and 0.1 for bubbly two-phase flows. The terms C_D, and A_i found in equation (2.4) are the drag coefficient and the interfacial area. These terms are, generally, provided by correlation. Any correlation can be used for these quantities, but the Ishii [6] correlation for the interfacial area is often used. It is shown in equations (2.8) and (2.9). This correlation is only appropriate for duct flow, since the hydraulic diameter of the channel is present. The α_{gs} term represents the void fraction in the small bubble region and d_b is the local bubble diameter.

$$A_i = \frac{4.5}{D}\cdot\frac{\alpha_g - \alpha_{gs}}{1-\alpha_{gs}} + \frac{6\alpha_{gs}}{d_b}\cdot\frac{1-\alpha_g}{1-\alpha_{gs}} \tag{2.8}$$

$$\alpha_{gs} = \begin{cases} \alpha_g & \text{for } \alpha_g < 0.25 \\ 0.3929 - 0.5714\alpha_g & \text{for } 0.25 \le \alpha_g < 0.6 \\ 0.05 & \text{for } 0.6 \le \alpha_g \end{cases} \tag{2.9}$$

It is important to show that the RPI model has a level of generality that permits the use of different correlations, which is noted by Kurul [2].

The crux of the RPI model is the wall heat flux partitioning. The wall heat flux is divided into three components:

1. The heat transferred to the liquid phase outside the zone of influence of the bubbles, q''_{1_ϕ}.
2. The heat transferred to the relatively cold liquid that fills the volume vacated by the detaching bubble, q''_Q.
3. The heat transferred to directly form the vapor, q''_e.

These components are shown in the following three equations.

$$q''_{1\phi} = A_{1\phi} h_{1\phi} \left(T_w - T_\delta\right) \tag{2.10}$$

$$q''_Q = t_Q f A_Q \frac{2k_l \left(T_w - T_\delta\right)}{\sqrt{\pi \mu_l t_Q}} \tag{2.11}$$

$$q''_e = \frac{1}{6} \pi d^3_{Bm} \rho_g h_{fg} f N_{sd} \tag{2.12}$$

Here A_{1_ϕ} is the fraction of the wall area that is affected by the presence of the bubbles and A_Q is the fraction that is not affected. The quenching heat flux, (2.11), was given by Del Valle and Kenning [7], where t_Q and f are the waiting period and the detachment frequency. T_w and T_δ are the temperatures at the wall and boundary layer thickness. Finally, d_{Bm}, and N_{sd} are the detachment bubble diameter and the number of nucleation sites per unit wall area. A_Q is given below.

$$A_Q = \pi d^2_{Bm} N_{sd} \tag{2.13}$$

There are four quantities that still need to be defined; the local bubble diameter, detachment bubble diameter, detachment frequency and the nucleation site density. The

detachment frequency and bubble diameter can be calculated by one of the many correlations available. The local bubble diameter and the nucleation site density have been found to be a function of local sub-cooling and wall superheat respectively. They are given by equations (2.14) and (2.15).

$$d_B = 10^{-4}\left(T_l - T_{sat}\right) + 0.0014 \quad [\text{m}] \tag{2.14}$$

$$N_{sd} = \left[210\left(T_w - T_{sat}\right)\right]^{1.8} \quad [\text{m}^{-2}] \tag{2.15}$$

The final piece of the model is the inter-phase mass transfer. There are two places that inter-phase mass transfer can occur, along the heated wall and in the bulk of the fluid. The evaporation of the liquid phase will only occur along the wall while, condensation of the vapor phase will occur throughout the entire domain. The degree of sub-cooling will dictate where the condensation occurs. The growing bubble will begin to condense immediately after its incipience when a large degree of sub-cooling is present. As sub-cooling decreases, the bubble penetrates further into the continuum of liquid and the coalescence of bubbles can occur before their condensation. When sub-cooling is equal to zero the bubbles do not condense, they only coalesce.

The vapor generation rate at the wall can be modeled by deriving an equation for the total mass of the detaching bubbles. Thus, the vapor generation rate is given as

$$\Gamma_g'' = \frac{q_e''}{h_{fg}} = \frac{1}{6}\pi d_{Bm}^3 \rho_v f N_{sd} \tag{2.16}$$

The condensation is determined by the amount of heat that is transferred to the continuous liquid phase from the disperse vapor phase. Thus the condensation rate is given by equation (2.17).

$$\Gamma''_{cond} = \frac{h_i\left(T_v - T_l\right)}{h_{fg}} \tag{2.17}$$

Here h_i is the interfacial heat transfer coefficient. The temperature of the vapor is often assumed to be the saturation temperature, so T_v is replaced with T_{sat}.

The correlation for the interfacial heat transfer coefficient was found not to effect the results drastically. Generally, the Wolfert [8] correlation is used,

$$h_i = \rho_l c_{pl} \sqrt{\frac{\pi}{4} \cdot \frac{\left|U_v - U_l\right|}{d_b} \cdot \frac{k_l}{\rho_l c_{pl}} \cdot \frac{1}{1 + \frac{k_l^t}{k_l}}} \tag{2.18}$$

where k_l, and k_l^t are the thermal conductivity and the turbulent conductivity of the liquid.

The evaporation of water will only occur at nucleation sites on the heated surface. This is true except when a rapid de-pressurization of the system occurs. In that case the water can flash to steam if the water's temperature is above the saturation temperature. The mass transfer term along the wall is modeled as shown in equation (2.19). Along the heated surface a "mass source" is added to the vapor equations and an equivalent "mass sink" is added to the liquid equations (2.1 through 2.3)

$$\Gamma_g = -\Gamma_l = \Gamma''_e A_{wall} - \Gamma''_{cond} A_i \tag{2.19}$$

This same equation holds true away from the wall by setting A_{wall} equal to zero. Thus, a mass source is added to the liquid equations and a sink to the vapor equation.

The RPI model does have certain limitations. First and foremost, it is only valid when applied to sub-cooled nucleate boiling. Once the fluid is heated to the saturation temperature the vapor generation rate is modeled in a non-mechanistic manner as

$$\Gamma_g'' = \frac{q_{wall}''}{h_{fg}} \tag{2.20}$$

The condensation rate would automatically go to zero according to equation (2.17). An appropriate correlation for interfacial area, that will account for the effect of bubble coalescence, needs to be provided.

The RPI model has been used and compared to experimental data. Kurul [9] compared the RPI model with a calculation using the drift flux model and with experimental data for duct flow. The calculations were performed for steady state and transient flows. The RPI model was found to predict the flow with a much greater degree of accuracy, especially near the wall. The drift flux model had a tendency to over predict the temperature and void fraction. The drift flux model also did not respond well during a transient.

The most impressive application of the RPI model is its use in determining the phase distributions in fuel assemblies. [10] Here the RPI model successfully predicted the void fraction at numerous locations within a BWR fuel assembly. The effect that spacers have on the void fraction and local pressure drop was also studied. The RPI model was used to predict two-phase pressure drop multipliers. The results compared well with the available experimental data. This study confirmed that the RPI model can properly predict the basic physics of two-phase flows in complex geometries. This is most important because the majority of situations that require CFD modeling will not be simple systems like a circular pipe.

2.1.1 TRAC/RELAP Model

TRAC and RELAP are codes used by the nuclear power industry for safety analysis. They are used to model the effect that a transient (disturbance) will have on the reactor system. Transients include any incident that would force the system to deviate from its steady state operating conditions. This includes anticipated operating occurrences and accidents. Such occurrences would include small and large break loss-of-coolant accidents, loss of flow accidents, loss of power, main steam line breaks, and control rod withdrawal, just to name a few. TRAC and RELAP have been continuously under development since the late 1960's. They are used worldwide and are regarded as industry standards.

The two codes are similar in many ways. Each solves the two-fluid equations and each accounts for interfacial mass, momentum, and energy transfer in a similar manner. However, they are dissimilar in one very important way; TRAC is capable of three-dimensional calculations while RELAP is one-dimensional.

Inter-phase momentum transfer is accounted for in each code. However, TRAC only accounts for the drag force, while RELAP accounts for the drag and the virtual mass forces. The exclusion or inclusion of the virtual mass term, however, does not represent a shortcoming of the TRAC code. It has been found (Drew [11] and Watanabe [12]) that the virtual mass term does not effect the solution of the problem, but it does enhance the stability of the numerical algorithm. Watanabe inserted the virtual mass term into TRAC and found that it stabilized the basic equations and the numerical calculations. It was also found that the CPU time was drastically reduced.

Inter-phase mass transfer is accounted for in an entirely different manner than the RPI model. TRAC (and RELAP) divide the mass transfer term into two quantities. The first is the vapor generation rate resulting from interfacial heat transfer, Γ_i, and the second is the vapor generation rate due to sub-cooled boiling, Γ_{sub}. The gas phase is assumed to be a homogenous mixture of vapor and noncondensable gas in thermodynamic equilibrium and is denoted by the subscript 'g'. The mixture is assumed to obey Dalton's law of partial pressure. The rate of change of energy of the gas phase is calculated by adding the energy transfer from the gas to the interface and the gas to the liquid. The opposite is done for the liquid phase. This allows the inter-phase mass transfer to be written as,

$$\Gamma_i = \frac{q_{ig} + q_{il}}{Vol_{cell}\left(h_v - h_l\right)} \tag{2.21}$$

where the sub-script 'v' is for vapor and

$$q_{ig} = \frac{P_s}{P} H_{CHTI}\left(T_g - T_{sv}\right) \tag{2.22}$$

$$q_{il} = H_{ALVE}\left(T_l - T_{sv}\right) + H_{ALV}\left\langle T_l - T_{sat}\right\rangle' \tag{2.23}$$

H_{CHTI} is defined as the vapor-side heat transfer factor, which is just the convection coefficient multiplied by the area term. Similarly, H_{ALVE} and H_{ALV} are the liquid-side heat transfer factor for evaporation/condensation and flashing, respectively. T_{sat} is the saturation temperature at total pressure and T_{sv} is the saturation temperature at steam partial pressure. The second term in equation (2.23) represents the flashing term and is set to zero if T_l is less than T_{sat}.

The vapor generation rate as a result of sub-cooled boiling is defined as

$$\Gamma_{sub} = \frac{q_{sub}}{Vol_{cell}\left(h_g - h_l\right)} \tag{2.23}$$

where the subscript 'g' is for the gas-steam mixture and q_{sub} will be discussed shortly. The wall heat transfer rate is given as

$$q_{wall} = h_\Gamma A_{wall}\left(T_w - T_l\right) \tag{2.24}$$

where h_Γ is the sub-cooled boiling heat transfer coefficient. To this point, the sub-cooled boiling model is not mechanistic; however, the method of determining h_Γ is. The Saha-Zuber [13] correlation is used to determine h_Γ (2.25). Saha and Zuber pointed out that sub-cooled boiling occurs in two regimes, thermally controlled and hydrodynamically controlled. The thermally controlled region was found to be for Peclet number less than 70,000 and the hydrodynamically controlled region is found beyond 70,000.

$$\begin{aligned} Nu &= 455 \quad \text{if Pe} \le 70{,}000 \\ St &= 0.0065 \quad \text{if Pe} > 70{,}000 \end{aligned} \tag{2.25}$$

These results are interpreted by Saha and Zuber as follows. [13] In the thermally controlled region, the bubbles stay attached to the walls until a characteristic roughness parameter (St=0.0065) is reached, at which point they detach from the surface. Since the sub-cooling is still high, the bubbles are forced to stay near the heated wall and flow down stream until the local Nusselt number becomes 455. At this point, the local sub-cooling is low enough to initiate a rapid increase in void fraction. In the hydrodynamically controlled region, the Stanton number reaches the value of 0.0065 at a point where the Nusselt number is already higher than 455. Thus, as soon as the bubbles

are detached from the wall they can move to the liquid core without condensing. This results in the rapid increase in vapor void fraction at the point of bubble detachment. This point is commonly referred to as the "point of net vapor generation".

If it is determined that sub-cooled boiling is occurring and the point of net vapor generation is reached, the wall energy is partitioned between the energy going into raising the temperature of the liquid and the energy going into vaporization. This is accomplished by the Lahey [14] mechanistic model. Lahey's model is shown in equation (2.26)

$$q_{sub} = q_{wall} \cdot \left(\frac{h_l - h_{ld}}{h_f - h_{ld}} \right) \tag{2.26}$$

where h_l, h_{ld}, and h_f are the liquid, point of departure, and saturation specific enthalpy. This model has been found to work well for nuclear applications, but it is too dependent upon empirical data to be considered truly mechanistic.

2.2 Two-Phase Turbulence Effects

The modeling of two-phase, turbulent flows is still in the development stage. In single-phase flows the κ–ε turbulence model is regarded as an industry standard; no such industrial standard exists for two-phase flows. Many studies have been conducted on two-phase turbulence effects, but very few offer general methods of modeling them.

In general there are five mechanisms, which are not independent of each other, that contribute to the turbulence modification in dispersed two-phase systems [15]:

1. Increase in apparent viscosity due to the presence of the bubble.
2. Shedding vortices or the presence of wakes behind the bubble.
3. Fluid moving with the particle as added fluid mass to the bubble.
4. Enhancement of the velocity gradients between two bubbles.
5. Deformation of the dispersed phase.

Effects one and two are considered the dominant mechanisms in turbulence modification, so the models offered, generally, attempt to model only these effects.

The effect of the dispersed phase on the turbulent kinetic energy depends on the ratio between the inertial and viscous forces. If the viscous force dominates, then the dispersed phase will follow the fluid's turbulent fluctuation. If the inertial force dominates, the particle's (or bubble's) trajectory is independent of the turbulent fluctuations of the fluid. The deviation of particle motion from that of the fluid generates a fluctuating relative velocity resulting in additional dissipation of energy due to shearing forces. [16]

These facts resulted in the κ–ε model for bubbly two-phase flow by de Bertodano [17]. The two-phase κ and ε equations are respectively shown below:

$$\alpha_l \frac{D\kappa_l}{Dt} = \nabla \cdot \left(\alpha_l \mu_t \nabla \kappa_l\right) + \alpha_l \left(\mu_t \left(\nabla \bar{\boldsymbol{u}} + \nabla \bar{\boldsymbol{u}}^T\right) : \nabla \bar{\boldsymbol{u}} - \varepsilon\right) + S_{ki} \tag{2.27}$$

$$\alpha_l \frac{D\varepsilon_l}{Dt} = \nabla \cdot \left(\alpha_l \frac{\mu_t}{\sigma_\varepsilon} \nabla \varepsilon_l\right) + \frac{\alpha_l}{\kappa / \varepsilon} \left(C_{\varepsilon 1} \mu_t \left(\nabla \bar{\boldsymbol{u}} + \nabla \bar{\boldsymbol{u}}^T\right) : \nabla \bar{\boldsymbol{u}} - C_{\varepsilon 2} \varepsilon\right) + S_{\varepsilon i} \tag{2.28}$$

Where the subscript 'l' represents the phase. The terms α, and μ_t are the volume fraction and the turbulent viscosity, respectively. The 'S' in the above equations represent source terms, and $C_{\varepsilon 1}$, $C_{\varepsilon 2}$, σ_ε are dimensionless constants.

Turbulence production is approximated by dividing the turbulent kinetic energy into two components: shear-induced and bubble induced. This approach of linear superposition for a non-linear process such as turbulence should only be considered an approximation. Using this approximation, de Bertodano found that the bubble induced turbulence production results in an additional source term in the two-phase 'κ' equation. The source term is shown in equation (2.29).

$$S_{ki} = \frac{\kappa_{Bl}}{\tau_d} = \frac{0.5\alpha_g C_{vm} \left|\overline{\boldsymbol{u}}_R\right|^2}{\left(\frac{2}{3} \cdot \frac{C_{vm}}{C_D}\right) \frac{d_b}{u_R}} \tag{2.29}$$

The denominator of equation (2.29) is a relaxation time constant and $\boldsymbol{u}_R$ is the relative velocity. C_D and C_{vm} are the drag and virtual mass coefficients, d_b is the bubble diameter.

The effect on the turbulent viscosity is also modeled assuming superposition holds. An additional term is used when calculating the turbulent viscosity. Sato [18] recommends the following equation,

$$\mu_l^t = C_\mu \rho_l \frac{\kappa_l^2}{\varepsilon_l} + \frac{1}{2} C_{\mu b} \alpha_v d_b \left|\boldsymbol{U}_v - \boldsymbol{U}_l\right| \tag{2.30}$$

where C_μ and $C_{\mu b}$ are 0.09 and 1.2 respectively. The first term in (2.30) is the standard formulation for turbulent viscosity, the later term represents the additional bubble induced viscosity.

The RPI model uses (2.30) when calculating turbulent viscosity. TRAC and RELAP do not solve the Reynolds averaged transport equations, they account for the turbulence effects through empirical data.

Additional work is necessary in the area of turbulence modeling of two-phase flows. A substantial amount of work has been performed in modifying the κ–ε model, but not much work has been done on other turbulence models, namely the Reynolds stress and Algebraic stress models. These models have been shown to predict turbulence in a more realistic manner than the κ–ε model. Despite their additional computational cost, they are being used more frequently for design work and should receive more attention in the future.

CHAPTER 3. APEX TEST FACILITY DESCRIPTION

The following facility description presented in sections 3.1 through 3.4 was taken verbatim from the "Quick Look Report for OSU APEX NRC-2 - *Station Blackout with Modified ADS Logic.*" [19]

The APEX test facility is a one-fourth height, one-half time scale, reduced pressure integral systems test facility. It accurately models the details of the AP600 geometry including the primary system, the passive safety systems, and parts of the non-safety grade chemical and volume control system and the normal heat removal system. The interconnecting pipe routings are also duplicated in the model. All of the primary system components are fabricated of stainless steel and are capable of prolonged operation at 400 psia and saturation conditions.

3.1 Primary System

The APEX primary system includes the following components:

- A reactor pressure vessel (RPV) that models the upper and lower reactor internals, the core barrel, the downcomer, and the core. Connections for the hot and cold legs and direct vessel injection (DVI) lines are provided. The RPV houses 48 electric heater rods each having a 1 inch (2.54 cm) diameter and a heated length of 36 inches (91.44 cm). The maximum core power is 600 kW.

- Reactor coolant loop piping that models two primary loops, each consisting of one hot leg and two cold legs. Break spool pieces have been installed on the hot and cold legs, the DVI line, and the core make-up tank's pressure balance lines (CMT-PBL) to simulate pipe breaks. The discharge from these valves vent to the break and automatic de-pressurization system measuring system (BAMS) to separate and measure break flow rates. BAMS is discussed in section 3.3.
- Two steam generators (SG), one on each loop, each having tube and shell dimensions scaled to simulate a Westinghouse Delta-75 SG.
- Four reactor coolant pumps (RCP), two attached to the lower channel head of each SG.
- A Pressurizer (PZR) with internal heaters capable of controlling pressure and minimizing pressure spikes in the reactor coolant system (RCS).

3.2 Passive Safety System

The APEX facility includes the following passive safety systems:

- Two core make-up tanks (CMT) each having a pressure balance line that connects the CMT head to the cold leg. Each CMT also has an injection line that permits draining of the CMT into one of two DVI lines connected to the reactor downcomer. Check valves and isolation valves have been included.

- An automatic de-pressurization system (ADS) that includes three valves off the top of the PZR, ADS1-3. The flow from ADS 1-3 is directed to a sparger that vents directly into the in-containment refueling water storage tank (IRWST). The ADS 1-3 flow nozzles are sized to represent two-trains of ADS 1-3 in the AP600. Fourth stage ADS is modeled by a single valve located off the top of each hot leg. The ADS 4 flow nozzles are sized to model two trains of ADS 4 on each hot leg in the AP600. Failure of the ADS 1-4 valves can be simulated by installing different flow nozzles.
- Two Accumulators pressurized with nitrogen to provide safety injection during de-pressurization events. Each accumulator has an injection line that connects to one of two DVI lines. Check valves and isolation valves have been included.
- An IRWST having two injection lines that connect to each DVI line. The IRWST is capable of being pressurized to 80 psia (0.55 MPa) to simulate containment backpressure. Return lines to the DVI lines are provided to represent containment sump recirculation lines.
- A passive residual heat removal (PRHR) heat exchanger is located inside the IRWST. The PRHR is driven by natural circulation. It draws liquid from one hot leg, rejects heat to the IRWST liquid, and returns cooled liquid into the lower channel head of one SG.

Figures 3.1 and 3.2 present schematics of the APEX Test Facility.

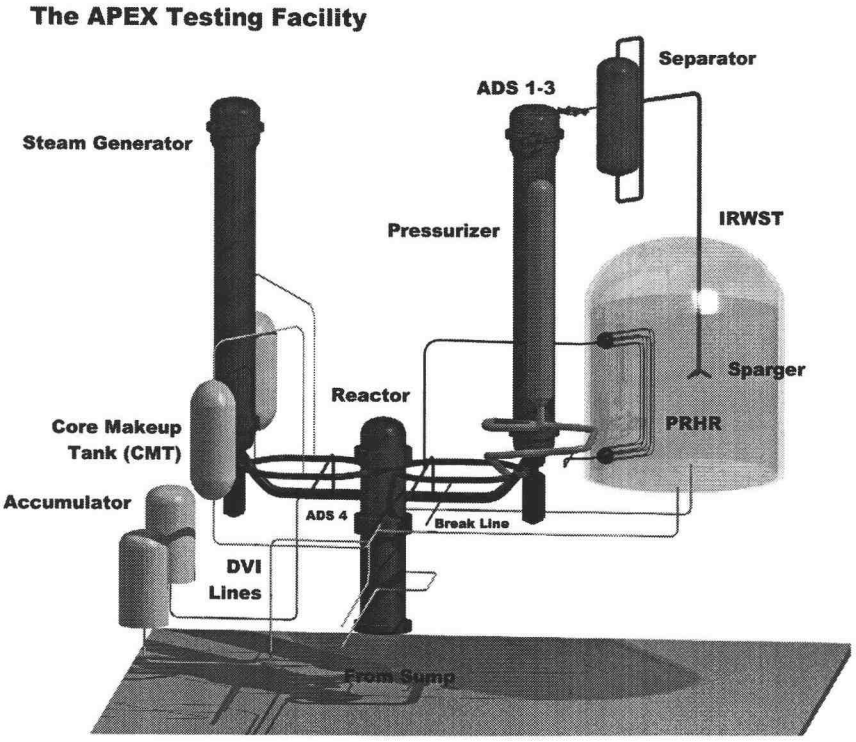

Figure 3.1: The APEX Test Facility

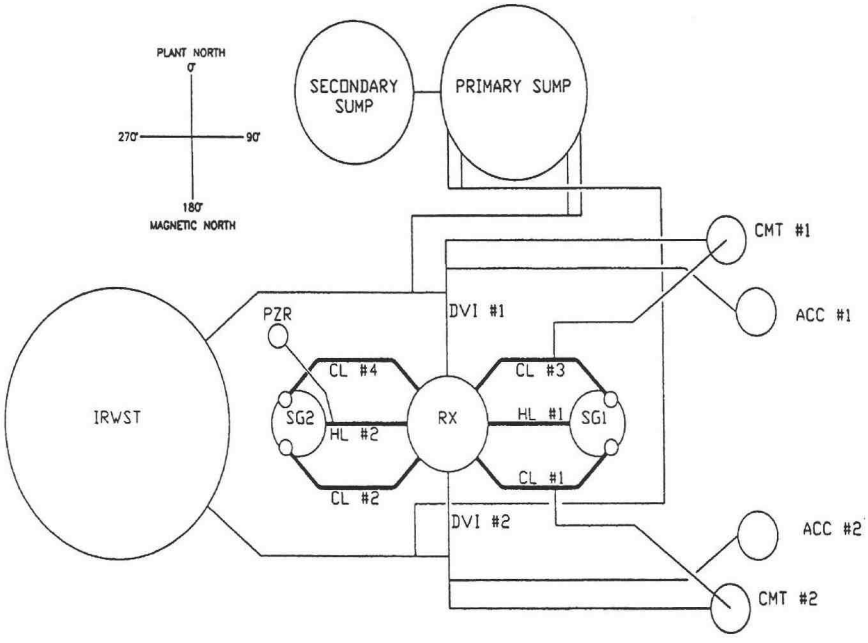

Figure 3.2: Schematic of APEX System

3.3 Break and ADS Measurement System (BAMS)

The BAMS is used to measure two-phase flows from breaks and the ADS measurement system. The two-phase flow is directed to a separator where the flow is separated into liquid and vapor. The liquid flow is measured and directed to the appropriate tank (IRWST or Primary Sump). The vapor flow is measured and vented from the test facility. Vapor flow from ADS 1-3 is directed into the IRWST. Electrical strip heaters are used to maintain boundary conditions at approximately 200°F (93.3°C). The system is capable of being pressurized to 80 psia (0.55 MPA) to simulate containment back-pressure.

The BAMS contains the following components:

- The Primary and Secondary Sumps - Simulate the containment compartment volumes below the normal floodup elevation. The primary and secondary sumps are connected with a line at a level simulating the curb overflow level in the AP600. The liquid overflow from the IRWST is also collected in the secondary sump. Both tanks are capable of being pressurized to 80 psia (0.55 MPA) to simulate containment back-pressure. Return lines to the DVI are connected to the primary sump to represent the containment sump recirculation lines.
- Four Moisture Separators - Three ADS separators and one break separator sized based on maximum expected flow rates. Separation is primarily accomplished by the use of gravity and a swirl vane moisture separator

element. Each separator is provided with a loop seal line on the liquid discharge to ensure vapor flow does not bypass the separator.

- Containment Sump Return System - Heated water from a hold-up tank is pumped into the Primary Sump and the IRWST at a mass flow rate equivalent to the mass flow rate of the vented steam. This heated liquid simulates the flow of condensate from the steam vented into the containment building. This steam would be condensed and drain into the IRWST or the containment (primary) sump.

3.4 Instrumentation

APEX includes the following types of instruments:

- Thermocouples (TF/TFM/TH/TW) are used to measure fluid temperatures. They are also used to measure the temperature distribution in the CMT walls and core heater rods. Premium grade thermocouples have been used and connected to the DAS through controlled purity thermocouple wire.
- Magnetic Flowmeters (FMM) are used to measure all single-phase liquid flow rates.
- Pressure Transducers (PT) are used to measure the static pressures within the various tanks and piping.
- Differential Pressure (DP) transducers are used to measure liquid levels in various tanks and piping. They are also used to determine pressure drops.

- Vortex Flowmeters (FVM) are used to measure all steam flow rates.
- Heat Flux Meters (HFM) are used to measure heat loss from individual tanks and components.
- Heated Phase Switches (HPS) are used to determine the fluid phase at various points inside system piping. Each HPS measures: 1) fluid temperature, 2) ΔT between the fluid and the heater, and 3) a relative heat transfer coefficient.
- Load Cells (LC) are used to measure the weight of liquid inside the IRWST, the Primary Sump, and the Secondary Sump.

Ambient air temperature and barometric pressure are also recorded. All of the instruments are monitored and recorded by the DAS (Data Acquisition System). Additionally, a sequence-of-events program is used to monitor various pumps and valves in the test facility.

3.5 Critical Components and Instrumentation

There are three components of the APEX facility that are of importance to this research. They are the PRHR, ADS-sparger and the IRWST. Both the PRHR and ADS-sparger are contained within the IRWST. The function of these components will be discussed further in the following sub-sections.

3.5.1 Passive Residual Heat Removal System

The function of the PRHR is to remove decay heat from the core in a passive manner during an emergency shutdown in which heat cannot be removed through the SGs or the RNS. A single PRHR system is installed in the APEX facility.

During an emergency shutdown, the PRHR isolation valve is opened allowing flow to leave Hot-leg-2 and enter the PRHR system. The flow enters the upper portion of the C-type heat exchanger that is mounted on the IRWST wall. The PRHR is shown in Figure 3.3. Heat is rejected from the tube-side flowing fluid into the IRWST fluid through natural convection and nucleate boiling. Figure 3.4 shows the direction of the flow.

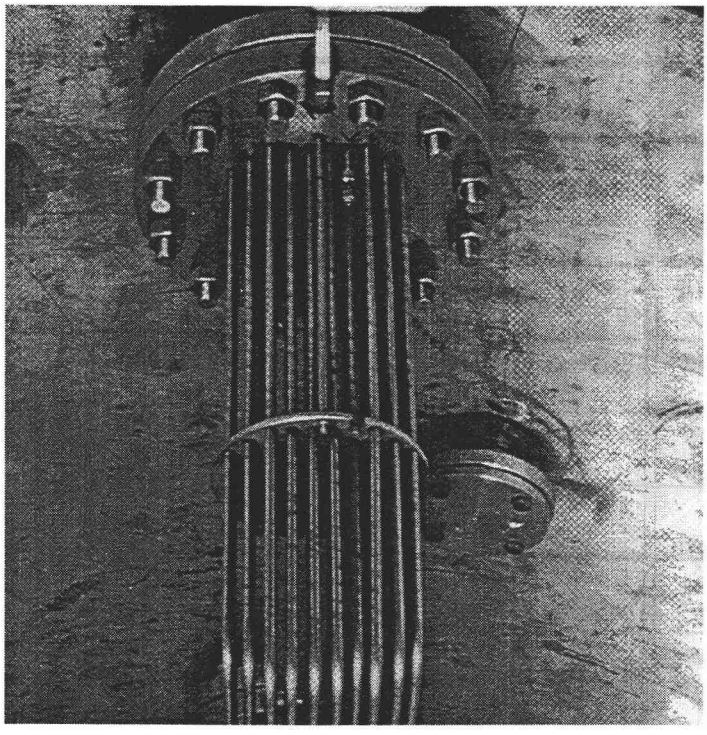

Figure 3.3: PRHR Heat Exchanger

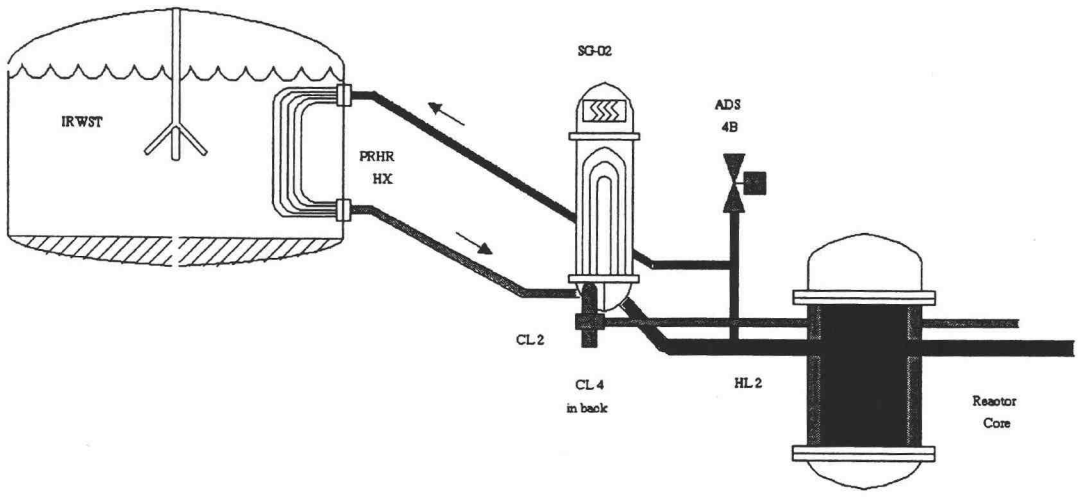

Figure 3.4: PRHR System Flow

The PRHR consists of the following instrumentation: magnetic flowmeters at the inlet and outlet; heat flux meters, two differential pressure meters to determine liquid level, and thermocouples to determine wall and fluid temperatures. The positions of the thermocouples are shown in Figure 3.5.

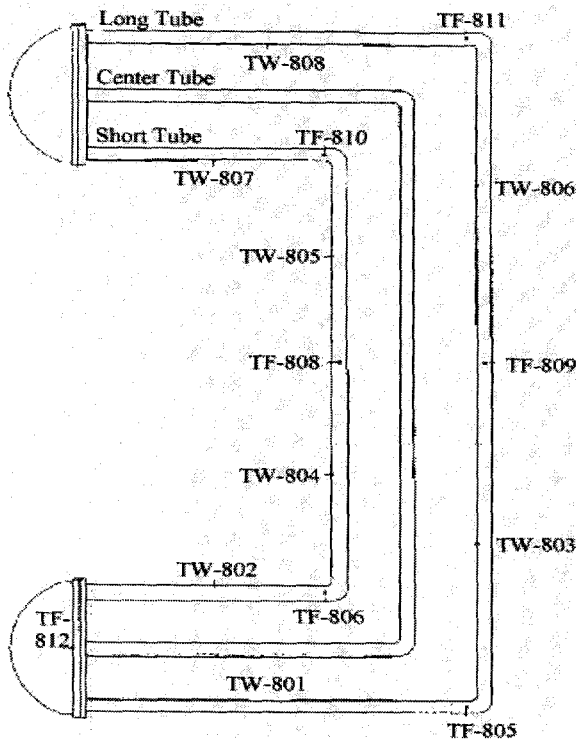

Figure 3.5: PRHR Instruments

3.5.2 Automatic De-pressurization System Sparger

The ADS sparger is a component of ADS 1-3. The function of the ADS is to reduce the system pressure by venting steam in a controlled manner, permitting the injection of cooling water from the CMTs, accumulators and the IRWST.

The ADS 1-3 is connected to the top of the pressurizer, and is a series of pneumatically operated ball valves, each of which are programmed to open at descending pressures. Thus, ADS-1 opens prior to ADS-2 and 3, and ADS-2 opens before ADS-3. The two phase flows vented through the valves are sent through a separator where the steam mass flow rates are then measured. The liquid and vapor are then recombined and vented into the IRWST through the sparger.

The sparger extends approximately half way down into the IRWST. At that point four arms extend from the sparger hub spreading out into the IRWST. Each of the sparger arms consists of 96 nozzles with a diameter of order 1mm. These nozzles act as buoyant jets to enhance the mixing of the ADS fluid and the fluid in the IRWST.

3.5.3 In-containment Refueling Water Storage Tank

The IRWST has numerous functions. It supplies the water that fills the refueling cavity when the plant is being refueled and stores this water during normal plant operation. The IRWST also provides emergency core cooling during an accident after the system has been de-pressurized. This occurs after the CMTs and accumulators have been exhausted. The final function of the IRWST is to act as the ultimate heat sink for the PRHR system during shutdown.

The IRWST holds approximately 4,000 gallons of water. It is capable of being pressurized up to 80 psi to simulate containment back-pressure. The IRWST is cylindrical with a hemispherical top and bottom. The hemispherical bottom is filled with a ceramic to simulate the flat bottom of the AP600. The water level never reaches the hemispherical top, because there is a vent that allows over flowing liquid to leave the IRWST. There are two discharge lines from the bottom of the tank. These discharge lines vent directly into the two DVI lines.

The instrumentation is limited to thermocouples, differential pressure, and load cells. Figure 3.6 shows the IRWST and the thermocouples that are found within it. The figure also shows the location of the PRHR and the ADS sparger.

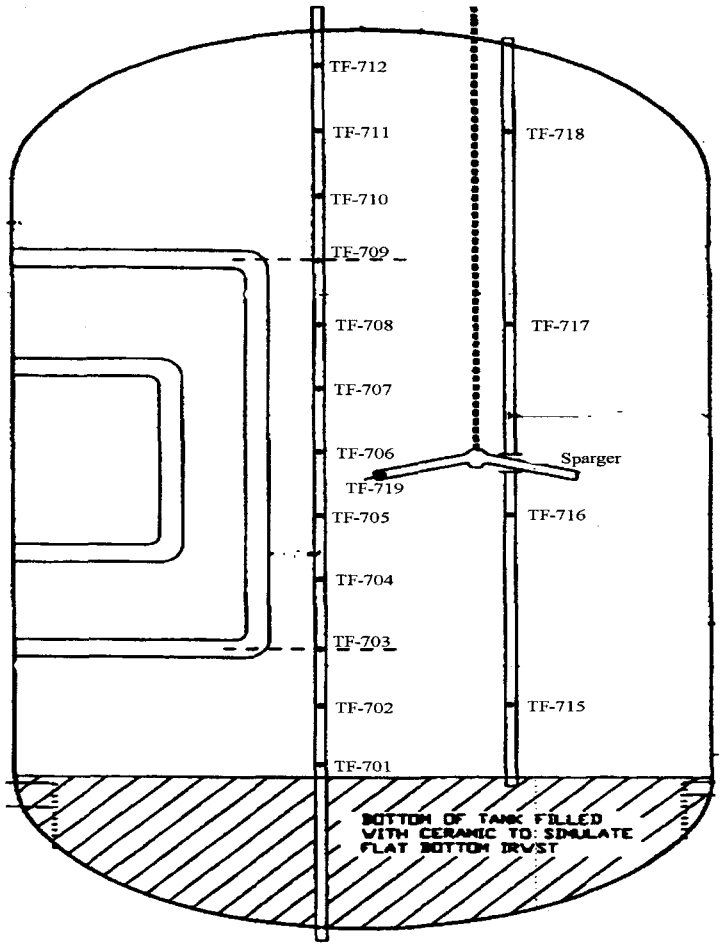

Figure 3.6: IRWST Instrumentation

Chapter 4. Description of Experiment

The primary purpose of the APEX test facility is to test the passive safety systems of Westinghouse's advanced light water reactor, the AP600. The passive systems must be capable of responding to numerous accident scenarios in accordance with all federal regulations regarding nuclear power plant safety. The facility is designed to model the actions of the passive systems in an identical manner as the actual AP600. The responses of the passive safety systems should be repeatable and follow the logic set by the AP600 design.

The APEX facility is unique because it is the only facility in the world that has the capability of studying the long term cooling phases of the AP600. These studies have lead to the observation of many unexpected phenomena, one of which occurred during the *Station Blackout Experiment.* The remainder of this chapter will describe the events that occurred during this experiment and why additional study was required.

4.1 Test Objectives

This test had three main objectives.[19] The first objective was to evaluate the long-term PRHR heat exchanger operation including the heat-up of the IRWST to saturation temperature. The second objective was to determine the effect that the saturated IRWST liquid had on system behavior during ADS 1-3 discharge. Finally, the effect on long term cooling caused by the injection of saturated liquid from the IRWST into the RPV was to be studied.

4.2 Test Description

This section presents a brief description of the *Station Blackout with modified ADS logic* test (NRC-5102). Prior to the initiation of the test all of the break valves are isolated from the system. These valves are used to simulate loss-of-coolant accidents (LOCAs) and should not be used during this experiment. The test begins with the simulated loss of AC power to the primary and secondary systems. The passive safety systems respond to the loss of power in five stages:

1. Secondary side blowdown phase
2. Natural circulation cooling phase
3. ADS blowdown phase
4. IRWST injection phase
5. Sump recirculation phase.

These phases occur in this order and are discussed in full detail in sections 4.2.1 through 4.2.5.

4.2.1 Secondary Side Blowdown Phase

This phase begins when the AC power is lost. The SG feed-water regulator valves are shut and the SGs are isolated. The reactor power is switched to decay mode and the pressurizer heaters are turned off. The reactor coolant pumps (RCP) are tripped after a set amount of time. At this point the system transitions to buoyancy driven natural circulation in the coolant loops. The coolant flows to the SGs through the hot legs and returns to the core, after it exits the SGs, through the cold legs. Heat is removed from the

system by the cyclic operation of the steam generator power operated relief valve (SG-PORV). The SG-PORV opens at 270 psig and closes when the pressure is reduced below 230 psig. This continues until the steam generator level drops below a set level. At this point a "S" signal is generated which opens the CMT pressure balance lines (CMT-PBL), CMT injection line, and PRHR heat exchanger isolation valves. The end of this phase sees a "S" signal set the ADS actuation signal on a timer for 415 minutes.

4.2.2 Natural Circulation Phase

This phase begins when the isolation valves for the PRHR, CMT-PBLs, and the CMT injection lines are opened. Immediately, natural circulation is established in the CMT-PBLs and the PRHR. Hot water flows up the CMT-PBLs into the head of the CMT which forces the relatively cold liquid in the CMTs to begin to drain through the injection lines. Similarly, hot water is taken from the hot leg and run through the PRHR, rejecting its heat into the IRWST and is then returned to the coolant loop through an injection pipe in the lower plenum of the steam generator. This phase is approximately seven hours long.

Heat is removed from the PRHR loop by the IRWST water. The IRWST water is initially at atmospheric pressure and approximately 288 K (60°F). The IRWST water is continuously heated for 25,000 seconds, during which, several thermally stratified layers develop in the tank. The thermal layer at the top of the tank reaches saturation at approximately 11,000 seconds, and the other thermal layers followed in approximately 3,000 second intervals, as is shown in figure 4.1.

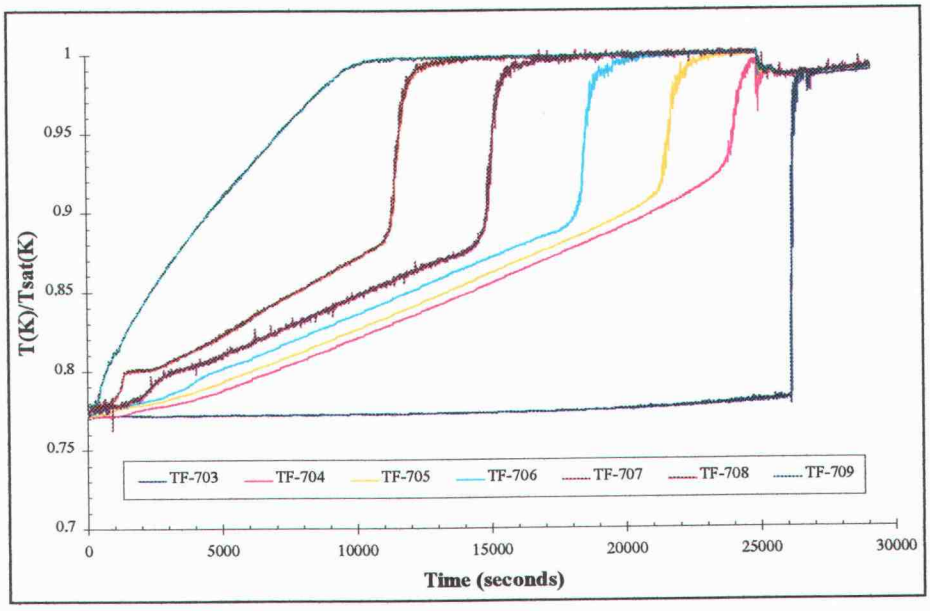

Figure 4.1: IRWST Fluid Temperature History

The total heat rejection by the PRHR is calculated by a simple energy balance. Figure 4.2 represents the normalized heat rejection history for the natural circulation phase. The time scale is off-set by the length of the secondary sub-cooled blowdown phase, so time zero is taken as the beginning of the natural circulation phase. As the figure shows, the heat removal rate decreases linearly with time.

The PRHR was divided into four zones to study the effectiveness of the different portions of the PRHR with respect to the heat removal. Figure 4.3 shows the layout of the four zones. It was determined [20] that the heat removal was not equal for each of the zones. Figure 4.4 shows the fraction of heat removed from each zone. As one can see the majority of the heat is removed from zone 1.

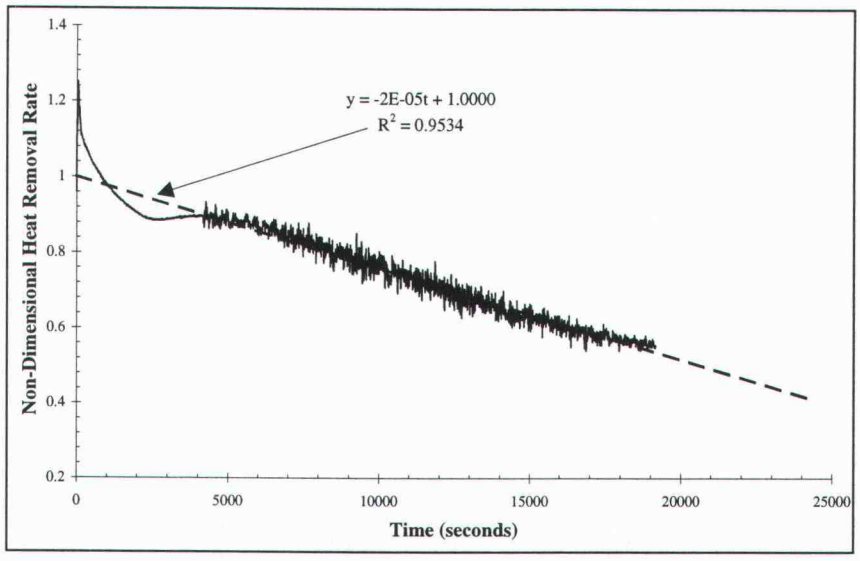

Figure 4.2: Heat Removal from the PRHR

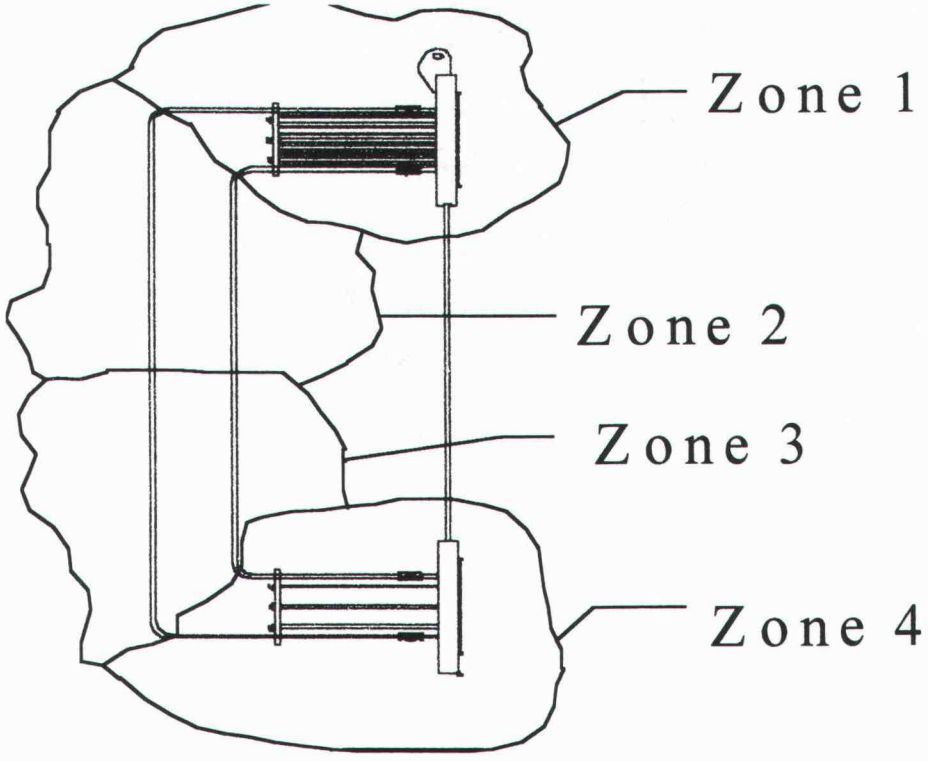

Figure 4.3: Map of the PRHR Heat Exchanger Zones

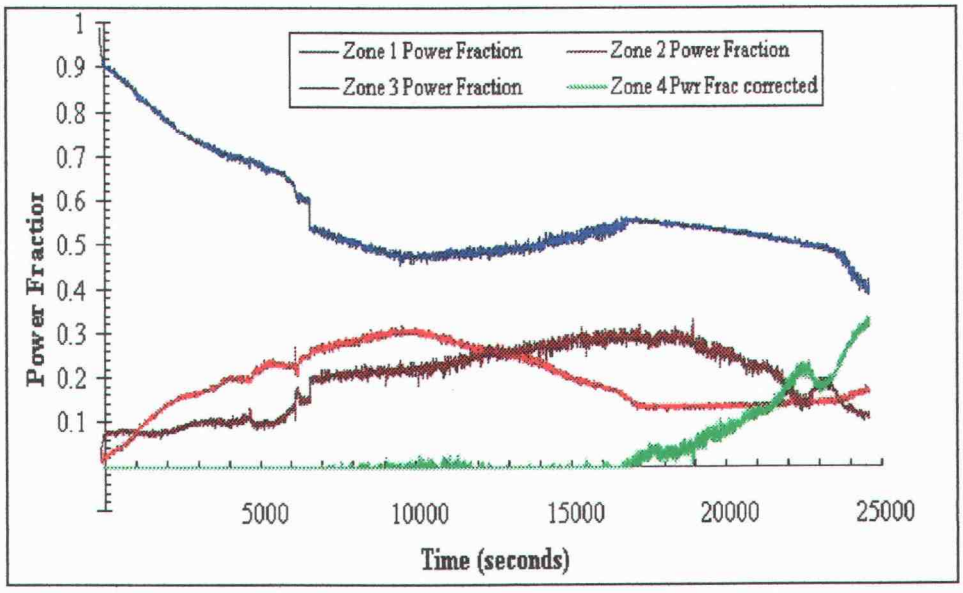

Figure 4.4: PRHR Zonal Heat Rejection Fractions

4.2.3 ADS Operation Phase

This phase started when the delay timer, set at the end of the first phase, reached 24,900 seconds (415 minutes) and an ADS actuation signal was issued. It ended when the system pressure reached the IRWST injection pressure. During this phase ADS 1, 2, and 3 actuate steam through the sparger into the IRWST. This de-pressurizes the primary system to nearly atmospheric pressure, and allows for the accumulators to completely empty.

The ADS 4 valves are then opened which leads to further de-pressurization, thus emptying the CMTs. Once the primary pressure is reduced below that of the IRWST, the check valve on the IRWST injection lines is opened permitting flow into the DVI lines and the IRWST injection phase begins.

4.2.4 IRWST Injection Phase

This phase begins when IRWST injection begins. It ended when flow was established from the containment sump to the RPV. This occurred when the IRWST liquid level reached 16.5 inches.

4.2.5 Sump Recirculation Phase

This phase began when the CSS-909 and CSS-910 valves were opened to equalize liquid level in the IRWST and the primary sump. After the levels equalized, a constant flow condition was established between the primary sump and the RPV.

4.3 Test Observations

Numerous observations were made during the station blackout experiment. The objectives set forth in section 4.1 were studied and the following conclusions were drawn.

1. The PRHR heat exchanger and CMT operation are capable of removing decay energy from the core for an extended period of time similar to that expected during a station blackout.
2. The ADS 1-4 blowdown was not significantly effected by the saturated conditions inside the IRWST.

3. The injection of the saturated IRWST liquid into the primary system did not impact the primary system pressure and as a result the IRWST was permitted to completely drain.

In addition to the aforementioned objectives, some unexpected phenomena were observed during the test. The unexpected phenomena were the large degree of thermal stratification exhibited by the tank and a peculiar flow pattern that developed in the tank. Each of these phenomena were found to effect the heat removal from the PRHR.

The thermal stratification can be attributed to the system geometry. The hot primary fluid enters the upper portion of the PRHR (zone 1) and rejects the majority of its heat before it enters the vertical section of the PRHR (zone 2). Figure 4.4 shows that on average zone 1 rejects of 60% of the heat. The heat being rejected flows up into the upper portions of the IRWST and collects there until saturation conditions are reached. At this point heat is transferred at two locations, the PRHR surface and the interface between the saturated layer and the sub-cooled layer. The heat transfer from the PRHR is through nucleate boiling, as previously mentioned. The mechanisms involved with the transfer over the interface are convection and conduction.

Figure 4.4 shows the heat rejected from zone 1 continuously decreases until approximately 11,000 seconds. This is approximately the same time that the saturated layer reaches the upper portion of the PRHR. At this point Figure 4.4 shows that the heat rejection from zone 1 begins to increase. This is not expected, since the effect of saturation has been found to decrease the nucleate boiling convection coefficients, hence decreasing the amount of heat that can be removed. It is suspected that the cause for this sudden increase lies with the heat transfer across the interface.

Aya *et al* [21] studied the heat transfer rates at the interface between a saturated layer and a sub-cooled layer. The study showed that with increasing sub-cooling the heat transfer coefficient increased exponentially. Figure 4.1 shows that a temperature difference (between the two thermal layers) of, approximately, 50 K exists. This is considered substantially sub-cooled and high convection coefficients can be expected.

The convection coefficient is also affected by the degree of near interface turbulence. Two independent studies of Thomas [22] and Murata *et al.* [23] showed that the transfer of turbulence over a steam/sub-cooled water interface enhances the condensation rate of the steam at the interface. The flow patterns observed contribute to the increase in turbulence, thus causing the saturated layer to grow within the IRWST.

These two effects can account for the rapid increase of temperature that is seen in Figure 4.1. They may also explain the increase in heat removal from zone 1. The heat transfer across the interface is primarily through direct contact condensation of the steam. This happens at such a high rate that the steam quality and void fraction in the saturated layer decreases, thus increasing the convection coefficient for zone 1. At the same time as the increase in heat removal from zone 1, there is a decrease in zone 2. Similarly, this is caused by the surrounding fluid's approach to saturation.

At approximately 18,000 seconds the heat removal from zone 1 begins to decrease once again. At this point the saturated layer has grown to engulf zone 2, and the increase in heat transfer at the interface can no longer effect zone 1. The effects are only felt in zone 2 and Figure 4.4 supports this with the slight increase of heat removal from zone 2.

4.4 Further Study

The effects of the phenomena mentioned in the previous section on the PRHR system are of importance, because they impact the efficiency of the PRHR and consequently effect the cooling behavior of the PRHR system.

The explanation given in the prior section is very speculative and for this reason further study is warranted. It is obvious that the effects can not be studied by a simple one-dimensional analysis. The effects of sub-cooled and saturated boiling and turbulence effects on condensation are all multi-dimensional phenomena and should be dealt with through a multi-dimensional analysis. The complexity of these effects prohibits an analytical study, so a computational study should be conducted.

This study lends itself to the use of a computational fluid dynamics (CFD) model. The recent advances in computer processing speed and the improvements in CFD techniques allow for the development of a reasonable model without sacrificing many important physical characteristics of the system.

The nuclear industry, unlike other industries, has limited experience with CFD techniques. This project will help bolster the validity of using such techniques for the nuclear industry in the future.

Chapter 5. CFX-4.2 Description

CFX-4.2 is a general, all-purpose three-dimensional CFD and heat transfer computer software suite. CFX-4.2 uses a control volume analysis to model a wide variety of flows, both simplistic and complex. The user interface is menu driven and allows model development in a quick and easy manner. CFX-4.2 was developed by AEA Technology of England.

Model development occurs on three levels: geometry and grid generation, flow solver setup, and graphic visualization. CFX-4.2's capabilities in these areas will be discussed in moderate detail throughout the remainder of this chapter.

5.1 Geometry and Grid Generation

The quality of a model begins and ends with the quality of the grid. This is the most important and often the most difficult aspect of CFD modeling. In this section, CFX-4.2's capabilities in this area are discussed.

Grids are characterized by the connectivity of their nodes. There are two types of grids, structured and unstructured. In a structured grid each node, generally, has the same number of neighboring nodes and the nodes are placed in a discernible logical pattern. In an unstructured grid this is not the case, each node can have any number of neighbors, and can be distributed in any order. Often the node distribution appears random, but of course it is not. The two different grid types have their advantages and disadvantages. The benefits of an unstructured grid is that it can be generated with very little, if any, user

interaction. It has the capability of being completely automated. This makes the grid generation of complex geometries easy. A structured grid generator does not have this luxury; some user interaction is required. A major disadvantage of unstructured grids is that they will require 10% to 15% more memory then a structured grid. This increase in memory requirement can be substantial for large problems. A major advantage of a structured grid is that the coding is less complex. Also, the majority of the development work in CFD has been performed with structured grids, they are well known and well tested. The current flow solver in CFX-4.2 is only capable of solving the transport equations on a structured grid, so the grid generators available are limited in that regard.

CFX-4.2 has two grid generators, MESHBUILD and BUILD. BUILD reads in three-dimensional CAD drawings and generates a grid for that geometry. This program could not be used for this research because there were no three-dimensional drawings of the APEX facility available. MESHBUILD is an interactive grid generator. The geometry is created and a grid is fitted to that geometry.

MESHBUILD uses the multi-block method of grid generation. This method involves dividing the physical domain into a series of interconnecting blocks. The blocks are connected through a shared face and information is passed from block to block through this face. Multi-block offers the capability of describing complex geometries with an "unstructured" block topology.

This method is beneficial because it offers the user more control over the grid. A single-block method would place stringent restrictions on the number of divisions an edge must have in order to resolve internal objects. This will often result in a large number of grid nodes for problems that do not require that degree of accuracy.

In order to demonstrate this method, lets consider a simple geometry of four circular pipes in a cross flow. Figure 5.1 shows the two different block topologies. Figure 5.1a is a single-block topology and 5.1b is a multi-block topology. The multi-block topology consists of 25 separate blocks. The advantage of multi-block becomes evident when the number of sub-divisions is set. For the single-block grid, the number of sub-divisions is only specified in two places, once on the vertical edges and once on the horizontal edges. The multi-block method allows the user to specify the number of sub-divisions in 10 different locations, five each on the horizontal and vertical edges. This allows the user to exercise greater control over the grid density distribution. The single-block method places restrictions on the number of edge sub-divisions. For this example, the number of sub-divisions must be a multiple of nine or the pipes will not be resolved properly within the grid. The multi-block topology is not restrained in anyway. Figure 5.2 show the two grids generated. Figure 5.2b has half as many cells and is a better quality.

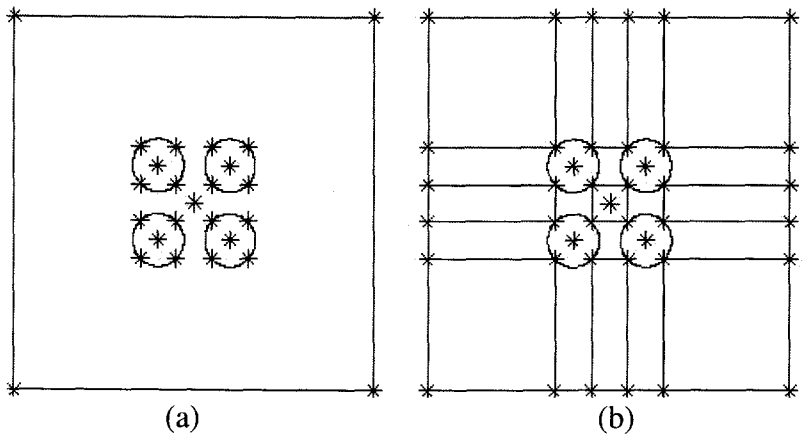

Figure 5.1: Single/Multi-Block Topology Comparison
(a) Single Block; (b) Multi-Block

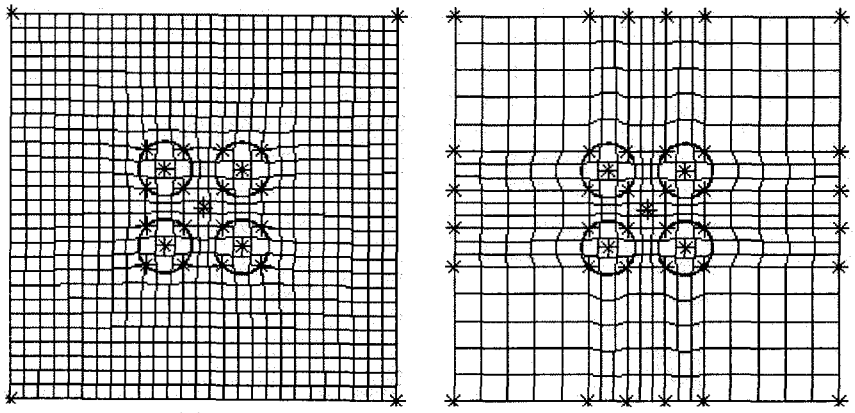

Figure 5.2: Single/Multi-Block Grid Comparisons
(a) Single Block; (b) Multi-Block

The advantages of multi-block grids can be better illustrated with complex geometries. When complex geometries are involved multi-block grids can save hundreds of thousands or perhaps millions of cells.

A grid in MESHBUILD can be generated with either algebraic or elliptical smoothing. Algebraic grid generation is the easier of the two methods. It simply entails the mapping of the boundaries into the physical domain through interpolation. A series of polynomial interpolation equations, often called projections, are written and the equations are then solved for the grid intersection points.

Elliptic smoothing is a generation technique that requires the solution of an elliptic partial differential equation (PDE). The solutions to an elliptic PDE are generally very smooth. Anderson *et al* [24] explains why, "Laplace's equation is a good choice for the elliptic PDE. To better understand the choice of Laplace's equation consider the solution of a steady state heat conduction problem in two-dimensions with Dirichlet boundary conditions. The solution of the problem produces isotherms that are smooth

and are nonintersecting. The number of isotherms in a given region can be increased by adding a source term. If the isotherms are used as grid lines, they will be smooth, nonintersecting, and can be densely packed in any region by controlling the source term."

Once the block topology has been specified the next step is to define the "patches". Patches are labeled regions of the problem geometry on which the user implements boundary conditions or specifies material properties. There are two-dimensional and three-dimensional patches. There are ten types of two-dimensional patches: inlet boundaries, mass flow boundaries, pressure boundaries, symmetry plane, walls, conducting boundaries, thin surfaces, inter block boundaries, periodic, and user2d. There are four types of three-dimensional patches: non-conducting solid, conducting solid, porous solid, and user3d.

The two-dimensional patches are set on block faces and the boundary information is stored at nodes at the center of the individual control volume faces. Three-dimensional patches are set on blocks and are not considered boundary conditions. Generally, they are used to add source terms into the transport equations through a user3d patch. A conducting solid patch specifies that only the heat diffusion equation is to be solved in this region.

The inlet flow into a system can be specified as an inlet or a mass flow boundary. At an inlet the velocity vector is specified and at a mass flow boundary the mass flow rate is set. The mass flow condition is especially useful when the flow can be considered fully-developed. The scalars (temperature, pressure, etc.) can also be set at the inlet or mass flow boundaries. A pressure boundary calculates the velocity at the boundary by a

specified pressure. If no patches are specified then all domain boundaries are considered adiabatic, no-slip walls.

A thin vessel boundary is just two walls placed back-to-back. This is because all two-dimensional patches are one-sided. Often it is desired to have a solid object within a flow field, i.e. pipes in a cross flow. These are often treated as thin vessels.

5.2 Flow Solver Options

CFX-4.2 [25] is capable of modeling numerous types of flows with the various options available through the flow solver. The flow calculations are based on the numerical solution of the Navier-Stokes equations. The analysis can be performed for steady state and transient situations. The flow solver is capable of solving non-isothermal problems by solving the energy transport equation. The system fluid can be either compressible or incompressible and there are models available for non-Newtonian fluids. There are numerous models available for the description of turbulent flows. The most popular of which is the κ–ε model. Buoyant flows are also capable of being solved through the Boussinesq approximation for incompressible flows.

CFX-4.2 has numerous options for more complex systems such as; multi-phase flows, combustion models, chemically reactive flows, particle transport models, flows through porous media, and a model for the Monte-Carlo simulation of radiation heat transfer.

The flow solver offers numerous options in the choice of the differencing schemes and linear equation solvers. There are also numerous options when describing

the velocity-pressure coupling and solution algorithm. All of these options provide the user with control over the numerical stability of the system.

The flow solver is applied to a colocated grid (all values are stored at the control volume center). The Rhie-Chow interpolation method is used to correct the problems associated with colocated or non-staggered grids, such as the sensitivity to the "checker-board" pressure field.

CFX-4.2 also supplies 31 different 'User FORTRAN' routines that can be used to implement options that are not offered by the current version of the code. One of these routines can be used to implement boundary conditions that vary with space and/or time. They can also be used to add complicated sources or sinks to the transport equations. The routines also allow the fluid properties to be described as a function of pressure and/or temperature.

5.2.1 Transport Equations

The transport equations for single and multi-phase flows are presented in this section. The single-phase transport equations are shown only for completeness and will not be discussed in great detail.

5.2.1.1 Single-Phase Equations

The system's vector and scalar fields are computed by seeking a solution to the three transport equations: mass continuity, momentum, and energy. It should be noted that the mass continuity equation can only be regarded as a transport equation in the case

of a compressible flow, in which it is the transport equation for density. The continuity equation is given as:

$$\frac{\partial \rho}{\partial t} + \nabla \cdot (\rho \boldsymbol{U}) = 0 \tag{5.1}$$

The momentum equation is given as:

$$\frac{\partial \rho \boldsymbol{U}}{\partial t} + \nabla \cdot (\rho \boldsymbol{U} \otimes \boldsymbol{U}) = \boldsymbol{B} + \nabla \cdot \sigma \tag{5.2}$$

where σ is the stress tensor given by:

$$\sigma = -p\delta + \left(\zeta - \frac{2}{3}\mu\right)\nabla \cdot \boldsymbol{U}\delta + \mu\left(\nabla \boldsymbol{U} + (\nabla \boldsymbol{U})^T\right) \tag{5.3}$$

The energy equation is written in terms of total enthalpy ($h+0.5\boldsymbol{U}^2$) and is given by:

$$\frac{\partial \rho H}{\partial t} + \nabla \cdot (\rho \boldsymbol{U} H) - \nabla \cdot (\lambda \nabla T) = \frac{\partial p}{\partial t} \tag{5.4}$$

Here ρ is the fluid density, $\boldsymbol{U}$ is the fluid velocity, p is the pressure, T is the temperature, h is the static enthalpy, and t is the time. The $\boldsymbol{B}$, μ, and ζ terms in the momentum equation are the body force, molecular viscosity and bulk viscosity respectively. The λ term in the energy equation is the thermal conductivity of the fluid.

The system of equations consists of five transport equations for seven unknowns: U, V, W, p, T, ρ, h. The system is closed by adding two equations. The first is an equation of state relating the density to temperature and pressure (i.e. ideal gas, Van der Waals). The ideal gas equation of state is only available in the present version, but different state equations can be implemented through user FORTRAN. For incompressible flow an equation of state is not needed, since density is assumed to be

constant. However, the user has the option of varying the density, on a cell basis, with temperature or pressure through user FORTRAN.

A constitutive equation for static enthalpy is also needed. The fluid is assumed to be thermally perfect, so static enthalpy only depends on temperature. The thermodynamic relation is given as:

$$C_p(T) = \left(\frac{\partial h}{\partial T}\right)_{p=const.} \tag{5.5}$$

The above equations are valid for laminar and turbulent flows, however, the solution of these equations for turbulent flow would require an extremely fine grid that would be capable of resolving the velocity fluctuations within and near the boundary layer. The current computational limitations prohibit the solution of the Navier-Stokes equations for turbulent flows, so the Reynolds averaged transport equations are used. These will be discussed in section 5.2.2.

5.2.1.2 Multi-Phase Equations

The multi-phase equations are applied to flows where there are more than one phase present. When using the multi-phase equations it is important to note the distinction between the continuous phase and the dispersed phase. The continuous phase occupies a connected region of space, while the dispersed phase represents disconnected regions within the continuous phase region.

In the case of a two-phase flow field the transport equations are written twice, one for each phase. The mass continuity equation is shown below.

$$\frac{\partial}{\partial t}\left(r_\alpha \rho_\alpha\right)+\nabla\cdot\left(r_\alpha \rho_\alpha \boldsymbol{U}_\alpha\right)=\sum_{\beta=1}^{N_p=2}\left(\dot{m}_{\alpha\beta}-\dot{m}_{\beta\alpha}\right) \tag{5.6}$$

Before proceeding to the remaining equations a few terms need to be discussed. The 'α' and 'β' subscripts refer to the different phases. The variable 'r_α' refers to the volume fraction of phase α. The volume fraction is defined as the ratio of the volume occupied by a phase to the total volume. Finally, the terms on the right-hand-side (RHS) of equation (5.6) represent the mass flow rate per unit volume caused by phase change. The subscript 'αβ' is read as the flow into phase α from phase β, like wise, 'βα' is read as the flow into phase β from phase α. All other symbols take the same meaning as those for the single phase equations except they apply to a particular phase.

The momentum and energy equations are given as:

$$\begin{aligned}\frac{\partial}{\partial t}\left(r_\alpha \rho_\alpha \boldsymbol{U}_\alpha\right)+\nabla\cdot\left(r_\alpha\left(\rho_\alpha \boldsymbol{U}_\alpha\otimes\boldsymbol{U}_\alpha-\mu_\alpha\left(\nabla\boldsymbol{U}_\alpha+\left(\nabla\boldsymbol{U}_\alpha\right)^T\right)\right)\right)&=r_\alpha\left(\boldsymbol{B}_\alpha-\nabla p_\alpha\right)\\ +\sum_{\beta=1}^{N_p=2}c_{\alpha\beta}^{drag}\left(\boldsymbol{U}_\beta-\boldsymbol{U}_\alpha\right)+\sum_{\beta=1}^{N_p=2}\left(\dot{m}_{\alpha\beta}\boldsymbol{U}_\beta-\dot{m}_{\beta\alpha}\boldsymbol{U}_\alpha\right)&+\boldsymbol{F}_\alpha\end{aligned} \tag{5.7}$$

$$\begin{aligned}\frac{\partial}{\partial t}\left(r_\alpha \rho_\alpha H_\alpha\right)+\nabla\cdot\left(r_\alpha\left(\rho_\alpha \boldsymbol{U}_\alpha H_\alpha-\lambda_\alpha\nabla T\right)\right)&=\sum_{\beta=1}^{N_p=2}c_{\alpha\beta}^{h}\left(T_\beta-T_\alpha\right)\\ +\sum_{\beta=1}^{N_p=2}\left(\dot{m}_{\alpha\beta}H_\beta-\dot{m}_{\beta\alpha}H_\alpha\right)&\end{aligned} \tag{5.8}$$

The second term on the RHS of equation (5.7) represents the interfacial transport caused by drag between the phases. The drag coefficient in this term is given by a variety of correlations. These and other correlations will be discussed further in section 5.2.3. The third term represents a momentum source/sink caused by phase change and the fourth term represents any other interfacial transfer mechanism that may be present.

The first term on the RHS of equation (5.8) represents the transport of heat between the dispersed phase and the continuous phase in thermal non-equilibrium conditions. The second term represents a heat source/sink caused by phase change.

For a two phase system of equations there are 16 unknowns: U_α, V_α, W_α, p_α, ρ_α, r_α, T_α, h_α (one for each phase), however there are only ten equations. Four additional equations are given through the phasic equations of state and constitutive equations. One additional equation is found by placing an algebraic constraint that requires the volume fractions to sum to unity. The system is closed by considering a relationship between the phasic pressures. The default is to assume that the phasic pressures are equal, but there is an option to include surface tension effects.

5.2.2 Turbulence Models

CFX-4.2 offers several options when modeling turbulent fluid flow. The remainder of this section will be devoted to describing the different turbulence models and how they influence the calculations. The models will be presented in the single-phase form and an additional section will show how the single-phase equations are generalized into multi-phase equations.

5.2.2.1 Reynolds Averaged Equations

Turbulent flows are extremely complex and time-dependent. They are governed by the Navier-Stokes equations but the required grid resolution makes it virtually

impossible to solve with the current technology. This has led to a turbulence modeling technique known as Reynolds averaging.

This idea behind this technique is to divide the velocity and scalar variables into two components, a mean value and a fluctuating value. Thus, the instantaneous velocity and scalar unknowns can be written as:

$$\begin{aligned} \boldsymbol{U} &= \overline{\boldsymbol{U}} + \boldsymbol{u}' \\ \Psi &= \overline{\Psi} + \psi' \end{aligned} \tag{5.9}$$

Here the bar represents a statistically averaged quantity. The variables marked with the 'prime' are the fluctuating components. The Ψ can represent any scalar quantity such as pressure, temperature, and enthalpy. The averaged quantity is calculated by the equation below:

$$\overline{\Psi} = \frac{1}{2\delta t}\int_{t-\delta t}^{t+\delta t} \Psi(\tau) d\tau \tag{5.10}$$

The Reynolds-averaged equations are derived by substituting equation (5.9) into equations (5.1), (5.2), and (5.4) and time averaging the equations term by term according to equation (5.10). This yields the following equations, respectively. If a more detailed description is required, Bejan [26] is suggested.

$$\frac{\partial \rho}{\partial t} + \nabla \cdot \left(\rho \overline{\boldsymbol{U}}\right) = 0 \tag{5.11}$$

$$\frac{\partial \rho \overline{\boldsymbol{U}}}{\partial t} + \nabla \cdot \left(\rho \overline{\boldsymbol{U}} \otimes \overline{\boldsymbol{U}}\right) = \boldsymbol{B} + \nabla \cdot \left(\sigma - \rho \overline{\boldsymbol{u}' \otimes \boldsymbol{u}'}\right) \tag{5.12}$$

$$\frac{\partial \rho \overline{H}}{\partial t} + \nabla \cdot \left(\rho \overline{\boldsymbol{U}} \overline{H} + \rho \overline{\boldsymbol{u}' h'} - \lambda \nabla \overline{T}\right) = \frac{\partial \overline{p}}{\partial t} \tag{5.13}$$

Now the total enthalpy includes a contribution from the turbulent kinetic energy which is given by equation (5.14), where the last term is the turbulent kinetic energy.

$$\overline{H} = \overline{h} + \frac{1}{2}\overline{U}^2 + \frac{1}{2}\overline{u'^2} \tag{5.14}$$

The averaging causes new terms to appear in the momentum and energy equations. These are commonly referred to as Reynolds stress (for the momentum) and Reynolds flux for the energy and other scalar equations.

There are nine components (three for each momentum equation) of the Reynolds stresses, as shown in equation (5.15)

$$\nabla \cdot \overline{\boldsymbol{u}' \otimes \boldsymbol{u}'} = \begin{cases} \left[\frac{\partial}{\partial x}\left(\overline{u'^2}\right) + \frac{\partial}{\partial y}\left(\overline{u'v'}\right) + \frac{\partial}{\partial z}\left(\overline{u'w'}\right)\right]\hat{i} \\ \left[\frac{\partial}{\partial x}\left(\overline{u'v'}\right) + \frac{\partial}{\partial y}\left(\overline{v'^2}\right) + \frac{\partial}{\partial z}\left(\overline{v'w'}\right)\right]\hat{j} \\ \left[\frac{\partial}{\partial x}\left(\overline{u'w'}\right) + \frac{\partial}{\partial y}\left(\overline{v'w'}\right) + \frac{\partial}{\partial z}\left(\overline{w'^2}\right)\right]\hat{k} \end{cases} \tag{5.15}$$

Similarly the Reynolds Flux is given in equation (5.16)

$$\nabla \cdot \overline{\mathbf{u}'h'} = \frac{\partial}{\partial x}\left(\overline{u'h'}\right) + \frac{\partial}{\partial y}\left(\overline{v'h'}\right) + \frac{\partial}{\partial z}\left(\overline{w'h'}\right) \tag{5.16}$$

The Reynolds stresses and fluxes offer nine additional unknowns. Closure for the system of equations can be reached by two different methods, the eddy viscosity model or second order closure models.

5.2.2.2 Eddy Viscosity Models

This method assumes that the Reynolds stresses and fluxes can be represented algebraically in terms of known quantities. This is done through the eddy viscosity

hypothesis, which states that the Reynolds stresses can be linearly related to the mean velocity gradients in a manner analogous to the relationship between stress and strain tensors in laminar Newtonian flow [25]. This allows for the Reynolds stresses and fluxes to be simplified into a constant multiplied by a velocity or scalar gradient. The constant is commonly referred to as the turbulent or eddy viscosity and diffusivity. Refer to Bejan [26] for further details.

CFX-4.2 offers four eddy viscosity type turbulence models. These models have been widely tested and used for many diverse applications. The models are: κ–ε, low Reynolds number κ–ε, Wilcox κ–ω , and the RNG κ–ε model.

The purpose of each of these models is to determine the turbulent viscosity. The κ–ε *model* solves two additional PDE's for the turbulent kinetic energy, κ, and turbulent dissipation rate, ε. These are then related to the turbulent viscosity by equation (5.17).

$$\mu_T = C_\mu \rho \frac{\kappa^2}{\varepsilon} \tag{5.17}$$

Here the coefficient, C_μ, is given the value 0.09. The transport equations for κ, and ε are:

$$\frac{\partial \rho \kappa}{\partial t} + \nabla \cdot (\rho \boldsymbol{U} \kappa) - \nabla \cdot \left(\left(\mu + \frac{\mu_T}{\sigma_\kappa} \right) \nabla \kappa \right) = P + G - \rho \varepsilon \tag{5.18}$$

$$\frac{\partial \rho \varepsilon}{\partial t} + \nabla \cdot (\rho \boldsymbol{U} \varepsilon) - \nabla \cdot \left(\left(\mu + \frac{\mu_T}{\sigma_\varepsilon} \right) \nabla \varepsilon \right) = C_1 \frac{\varepsilon}{\kappa} \left(P + C_3 \max(G,0) \right) - C_2 \rho \frac{\varepsilon^2}{\kappa} \tag{5.19}$$

Where P, and G are the turbulent kinetic energy production due to shear and body forces respectively. C_1, C_2, C_3, σ_ε, and σ_κ are dimensionless constants with the values of 1.44, 1.92, 1.0, 1.3, and 1.0 respectively.

The *low Reynolds number* κ–ε *model* is a modification of the standard κ–ε model to allow calculation of turbulent flows with Reynolds numbers in the range 5,000 to 30,000. The model involves a damping of the turbulent viscosity. A modified definition of ε is used so that its value goes to zero at the walls. For further details on this model see Launder and Sharma [27].

The *Wilcox* κ–ω *turbulence model* is an alternative for the low Reynolds number κ–ε model. In this model, an equation is still solved for κ, but the equation for ε is replaced by an equation for the turbulence frequency ω, which is defined by $\omega=\varepsilon/\kappa$. This model can improve the prediction of turbulence in adverse pressure gradient boundary-layers.

The final eddy viscosity model available is the *RNG* κ–ε *model.* This model is an alternative to the standard κ–ε model for high Reynolds number. The only difference is that the constant C_1 is not considered constant, but is a function of turbulent kinetic energy and dissipation.

5.2.2.3 Second Order Closure Models

These types of models are often called Reynolds stress models. Instead of invoking the eddy viscosity hypothesis, the individual components of the Reynolds stress are computed. CFX-4.2 offers two such models: differential stress, and algebraic stress. These models are the most complex and complete closure models currently being used.

The *Reynolds stress* or *differential stress model* uses six PDEs to model the different turbulent stresses. In addition to these six equations, an equation is used to

determine the turbulent dissipation. Seven PDEs in addition to the five transport equations makes this model computationally expensive. For this reason it is not used in too many engineering applications, but as computer speed continues to increase this model will be used more. An excellent reference for this model is a book by Versteeg and Malalasekera. [28]

The *algebraic stress model* is similar to the Reynolds stress model in that it attempts to model the individual components of the turbulent stresses. Algebraic relations are solved for these stresses instead of PDEs. "This is an economical way of accounting for the anisotropy of the Reynolds stresses without going into the full length of solving the Reynolds stress transport equations." [28]

5.2.2.4 Multi-Phase Turbulent Flows

CFX-4.2 offers multi-phase versions of each of the single-phase turbulence models, but does not suggest that any of them are complete. Each of the models will have shortcomings when modeling multi-phase flows.

In a simple unmodified multi-phase κ–ε model, it is assumed that the eddy hypothesis holds for each turbulent phase; hence molecular and turbulent diffusion of momentum is governed by an effective viscosity:

$$\mu_{\varepsilon,eff} = \mu_\alpha + \mu_{T\alpha} \tag{5.20}$$

where

$$\mu_{T\alpha} = C_\mu \rho_\alpha \frac{\kappa_\alpha^2}{\varepsilon_\alpha} \tag{5.21}$$

The transport equations for κ and ε are assumed to take the same form as a generic advection-diffusion equation.

$$\frac{\partial}{\partial t}\left(r_\alpha \rho_\alpha \kappa_\alpha\right) + \nabla \cdot \left(r_\alpha \left(\rho_\alpha U_\alpha \kappa_\alpha - \left(\mu_\alpha + \frac{\mu_{T\alpha}}{\sigma_\kappa} \right) \nabla \kappa_\alpha \right) \right) = r_\alpha S_{\kappa\alpha} + \sum_{\beta=1}^{N_p} c_{\alpha\beta}^{(\kappa)} (\kappa_\beta - \kappa_\alpha) + \sum_{\beta=1}^{N_p} (\dot{m}_{\alpha\beta}\kappa_\beta - \dot{m}_{\beta\alpha}\kappa_\alpha) \tag{5.22}$$

$$\frac{\partial}{\partial t}\left(r_\alpha \rho_\alpha \varepsilon_\alpha\right) + \nabla \cdot \left(r_\alpha \left(\rho_\alpha U_\alpha \varepsilon_\alpha - \left(\mu_\alpha + \frac{\mu_{T\alpha}}{\sigma_\varepsilon} \right) \nabla \varepsilon_\alpha \right) \right) = r_\alpha S_{\varepsilon\alpha} + \sum_{\beta=1}^{N_p} c_{\alpha\beta}^{(\varepsilon)} (\varepsilon_\beta - \varepsilon_\alpha) + \sum_{\beta=1}^{N_p} (\dot{m}_{\alpha\beta}\varepsilon_\beta - \dot{m}_{\beta\alpha}\varepsilon_\alpha) \tag{5.23}$$

The source terms in the above equations are the same as in the single phase equations.

The default is to set the interfacial transfer terms (second term on the RHS) to zero, since there is no reasonable and general way to model these quantities. Users can input their own models if they wish through user FORTRAN.

In most situations, there will be additional production and dissipation of turbulence not captured by the single-phase source terms. It is recommended that the user add source terms to account for these effects through user FORTRAN.

CFX-4.2 offers an option to include the bubble induced viscosity term by Sato [18]. The extra term is added to equation (5.20) for the continuous phase and is given the form

$$\mu_{T\beta} = C_{\mu b} \rho_\alpha r_\beta d \left| \boldsymbol{U}_\beta - \boldsymbol{U}_\alpha \right| \tag{5.24}$$

where d is the bubble diameter. The viscosity of the dispersed phase is then given as

$$\mu_{\beta,eff} = \mu_{\alpha,eff} \frac{\rho_\beta}{\rho_\alpha} \tag{5.25}$$

The multi-phase versions of the Reynolds stress models implemented in the code are straightforward generalizations of the single-phase equations, again with zero inter-phase transport terms.

5.2.3 Multi-Phase Interfacial Relations

All of the multi-phase transport equations have interfacial transfer terms on the RHS of the equation. In section 5.1, it was stated that the quality of a model begins and ends with the quality of the grid. To a lesser extent the same can be said about the interfacial transport terms. By choosing the proper terms the accuracy of a model can be improved drastically. By the same token, inappropriate choices of interfacial terms can be devastating to the accuracy of the model.

CFX-4.2 offers several built-in options in describing the mass, momentum, and energy transfer terms. These terms are divided into four groups: drag forces, non-drag forces, inter-phase heat transfer, and inter-phase mass transfer. These are discussed further in the following sections.

5.2.3.1 Inter-Phase Drag

The second term of equation (5.7) accounts for inter-phase drag. The coefficient that appears in this term needs to be defined. Knowing that the drag exerted by a single particle on the continuous phase is:

$$\boldsymbol{D}_p = \frac{1}{2} C_D \rho_\alpha A \left| \boldsymbol{U}_\beta - \boldsymbol{U}_\alpha \right| \left(\boldsymbol{U}_\beta - \boldsymbol{U}_\alpha \right) \tag{5.26}$$

Hence the total drag per unit volume on the continuous phase is:

$$\boldsymbol{D} = n_p \boldsymbol{D}_p = \left(\frac{6 r_\beta}{\pi d^3} \right) \frac{1}{2} C_D \rho_\alpha A \left| \boldsymbol{U}_\beta - \boldsymbol{U}_\alpha \right| \left(\boldsymbol{U}_\beta - \boldsymbol{U}_\alpha \right) \tag{5.27}$$

where n_p is the number of particles per unit volume. Comparing equation (5.27) with the second term in equation (5.7) it can be shown that the coefficient can be written as:

$$c_{\alpha\beta}^{drag} = \frac{3}{4} C_D r_\beta \rho_\alpha \left| \boldsymbol{U}_\beta - \boldsymbol{U}_\alpha \right| \tag{5.28}$$

The only quantity that needs to be calculated is the drag-coefficient, C_D. There are several correlations that are available through CFX-4.2.

There are five flow regimes that can be described through the command language: viscous, Newton, distorted, spherical cap, and Ergun. There is also an option that allows the code to choose the flow regime automatically. This is the best option when the conditions of the flow are not known. The automatic option has limitations in that it can only use the viscous, distorted, or spherical cap models for fluid particles.

The drag-coefficient correlations available are: Schiller and Nauman [29], Ishii and Zuber[30], and the Ihme *et al* [31]. When there are high particle concentrations, many of the drag correlations should be modified to allow for the interactions between the particles. The only method currently available for fluid particles is the mixture viscosity method by Ishii and Zuber [30].

5.2.3.2 Non-Drag Forces

There are four inter-phase non-drag forces in the current version of CFX-4.2. They are: virtual mass force, lift force, wall lubrication force, and a turbulent dissipation force. Each of these forces were discussed in the description of the RPI model and are shown in equations (2.5) through (2.7), except for the wall lubrication force which is shown below.

$$\boldsymbol{F}_{\alpha} = \frac{r_{\beta}\rho_{\alpha}\left(\boldsymbol{U}_{\beta} - \boldsymbol{U}_{\alpha}\right)^{2}}{d} \cdot \max\left(-0.01 + 0.05\frac{d}{y_{w}}, 0\right)\boldsymbol{n} \tag{5.29}$$

Here d is the bubble diameter, y_w is the distance from the wall, and $\boldsymbol{n}$ is the normal to the wall. This force is in the normal direction away from a wall and decays with the distance from a wall. This force, generally, only exists in a region less than five particles from a wall.

5.2.3.3 Inter-Phase Heat Transfer

The inter-phase heat transfer term is the first term on the RHS of equation (5.8). This term represents the heat transfer across the interfacial boundary between the two phases. The rate of heat transfer per unit time across an interface of area, A_i, from phase β to phase α is given by:

$$Q_{\alpha\beta} = h_{\alpha\beta} A_{\alpha\beta}\left(T_{\beta} - T_{\alpha}\right) \tag{5.30}$$

where $Q_{\alpha\beta}$ is the heat transfer per unit volume, $A_{\alpha\beta}$ is the interfacial area per unit volume, and $h_{\alpha\beta}$ is the heat transfer coefficient. A comparison between equation (5.30) and (5.8) shows that

$$c^{h}_{\alpha\beta} = h_{\alpha\beta} A_{\alpha\beta} \tag{5.31}$$

The only quantity that needs to be calculated is the heat transfer coefficient, $h_{\alpha\beta}$. These are given through two correlations: Ranz and Marshall [32] and Hughmark [33]. These correlations have performed well in the past, but the user can implement any correlation through user FORTRAN if they wish.

5.2.3.4 Inter-phase Mass Transfer

The inter-phase mass transfer appears on the RHS of every transport equation. This term describes the total mass entering or exiting a phase, caused by phase change or by a source. CFX-4.2 allows for the user to introduce any mass transfer model through user FORTRAN.

The only built-in feature is the RPI sub-cooled boiling model. This model is implemented in a similar manner as was discussed in chapter 2.1, so it is not presented again.

5.2.4 Numerical Algorithm

The solution algorithm that CFX-4.2 applies to the transport equations is described in this section. The complete set of equations cannot be solved by a direct

method because of the excessive computational effort, and the fact that this approach ignores the non-linearity of the underlying equations. For this reason an iterative approach must be taken. The iterations occur on two levels: an inner iteration to solve for the spatial coupling of each variable; and an outer iteration to solve for the coupling between the variables.

The computational procedure is described in the next few paragraphs and is laid out in Figure 5.3. The first step is to set an initial field for all variables: U, V, W, p and T etc. Once an initial field is set, the discrete transport equations for the velocities can be formed separately by regarding all other variables as fixed. They are in turn sent to a linear equation solver, which returns the updated values. This is the so-called inner iteration.

There are several different linear solvers available. They are: line relaxation, preconditioned conjugate gradients, Stone's full field solve, block Stone's method, and the algebraic multi-grid method (AMG). AMG is recommended for complex geometries.

Generally, the velocities that have just been computed do not satisfy the mass continuity equation. This is because the pressure field is not correct. However, a pressure field is needed that will satisfy continuity The treatment of pressure is slightly different since it does not obey a transport equation like the other variables. The correct pressure field is obtained through one of the velocity-pressure coupling algorithms. The algorithm takes a simplified version of the discrete momentum and mass continuity equations and derives a pressure correction equation, which is solved via a linear equation solver. This pressure correction term is then used to update the pressure and velocity-components by adding the corrections to their previous value.

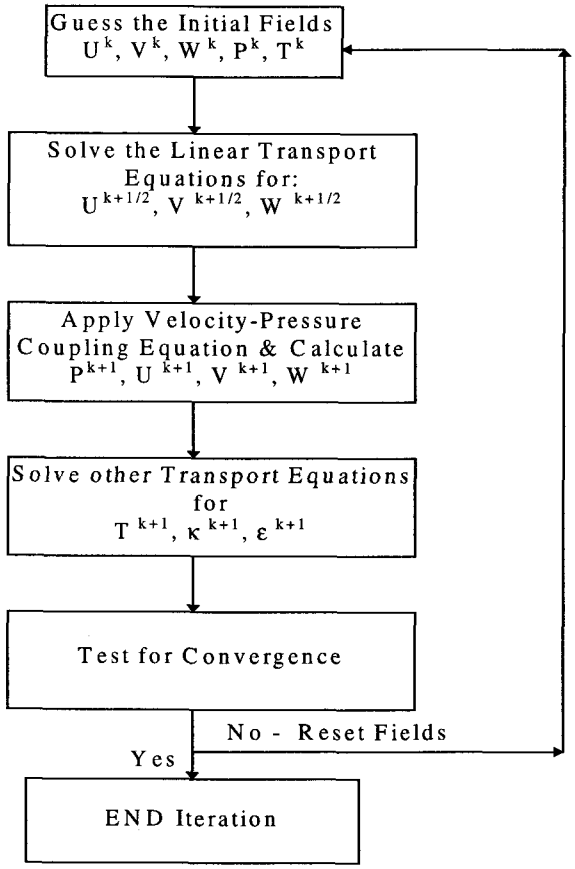

Figure 5.3: Computational Flow-chart

Under-relaxation is employed when correcting these terms to ensure greater numerical stability. This is accomplished by multiplying the correction terms by a under-relaxation factor between zero and one.

After the pressure and velocities have been updated the remaining scalar equations (energy, and turbulence equations) are solved with these updated values. Once all the transport equations have been solved, the variables are tested for convergence. If convergence of the variables is not reached, the process is repeated. This is done by setting the current values of the variables to the initial values and marching through the same procedure again. This is the so-called outer iteration.

CFX-4.2 offers three velocity-pressure coupling algorithms: SIMPLE, SIMPLEC, and PISO. The SIMPLE algorithm was the first of these methods to be developed and the latter two are merely improvements upon it. SIMPLE and SIMPLEC are both designed to be iterative methods. PISO is designed to be a semi-implicit non-iterative method. Once again reference [28] is recommended for a more in-depth description.

5.3 Graphical Visualization

CFX-4.2 has three post-processing programs: CFX-View, CFX-Linegraph, and CFX-Visualize. CFX-View and Visualize perform most of the same tasks, but CFX-Visualize is slightly more user-friendly. The types of plots that can be produced are: two-dimensional slice plots, vector and streamline plots, contour plots, plots of patch information, isosurface plots, line graphs, and probe plots.

CFX-Visualize has a line graph plotter that allows for multiple line graph plots, generated in Visualize, to be viewed on the same the graph. CFX-Visualize, also, has an additional function that allows the viewing of two-dimensional animation files, CFX-View does not. However, CFX-View can display particle track plots, while CFX-Visualize cannot.

CFX-Linegraph is used to produce line graphs for transient flows. In the command language the user can set monitoring points and have information written to a file as a function of time.

Chapter 6. IRWST/PRHR Model

The IRWST model went through many stages of development from beginning to end. Some aspects of the model were simplified which allowed for a more detailed analysis of the other components of the model. This chapter is divided into three sections describing the IRWST model. The first section presents the preliminary work that allowed various simplifying assumptions in the final model. The second section presents the final model and the results from the simulation. The third and final section will briefly discuss the errors inherent in the computational analysis and the errors associated with the assumptions made in the final model.

6.1 Preliminary Model

The preliminary development of the IRWST model consisted of a single phase approximation. The entire geometry was modeled including the ADS sparger and the PRHR heat exchanger, each of which are housed in the IRWST. The PRHR heat exchanger consists of a bundle of tubes that has the primary fluid passing through the tube side and the IRWST fluid on the outside. When compared to the size of the IRWST, these tubes are extremely small. This fact makes it impossible to model each and every tube in the bundle, so the PRHR is modeled as a single pipe.

The ADS sparger is also considered in this model. The nozzles on the sparger arms that allow for steam actuation into the IRWST were not considered. These nozzles

are only important during the portion of the experiment when the ADS is activated and otherwise are not of any significance.

6.1.1 Geometry and Grid

The current geometry consisting of the sparger and the PRHR is extremely complex. This is caused by the sparger arms, which extend off at angles into the IRWST. To generate a grid for this geometry, it was necessary to divide the system into 296 blocks. An over-head view of the blocking network is shown in Figure 6.1. A side view would offer no insight into the block layout because it is too cluttered with lines, so it is not shown. The vertical section (into the paper) of the IRWST is divided into eight levels. A level is created whenever the PRHR or sparger changes in shape and direction. In the first and last level there is no PRHR present, just the sparger and it's support pipe. Two levels are needed to represent the top and bottom PRHR horizontal sections. The remaining sections transverse the vertical sections of the PRHR and are needed because of changes in the sparger thickness.

There were many constraints on this geometry that affected the grid generation. They all involved the blocks around the sparger. The representation of the sparger arms leads to these constraints. The arms are smaller than the sparger hub to which they are attached, so they must be constrained within a larger block. This was done instead of using a multi-block layout because multi-block would require nine blocks to resolve one sparger arm. These nine blocks would propagate throughout the entire domain on the same level as the sparger arms. This would have increased the number of blocks

drastically and this would have pushed the memory limits of the workstation. Figure 6.2 shows the grid. The grid consists of 57,224 cells.

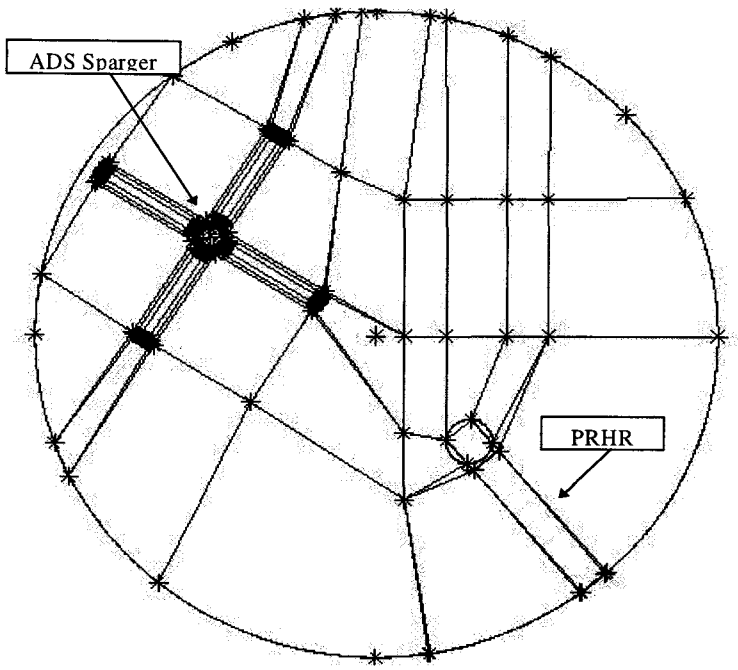

Figure 6.1: Block Network of Preliminary IRWST Model

A high quality grid exhibits several properties; the two most important are orthogonality of the grid line intersections and a general smoothness of the cell distribution. The grid shown in Figure 6.2 is highly orthogonal, but the cell distribution goes through rapid changes in nodal density, hence the grid is un-smooth at certain locations. This has a tendency to introduce errors into the numerical computation. However, a solution to this problem could not be found because of the geometric complexity. The only solution would be to use more blocks, which is not viable since the current block layout is pressing the memory limits of the machine.

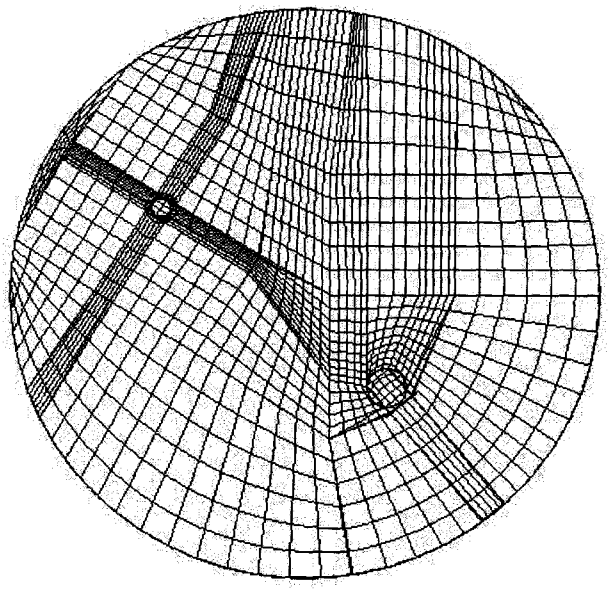

Figure 6.2: Grid for the Preliminary IRWST model

6.1.2 Flow Model

Several assumptions were made in development of this preliminary model. The most important of which are discussed below.

1. The heat flux on the surface of the PRHR can be prescribed from the experimental data, thus ignoring its dependence on the fluid passing through the tube side of the PRHR.
2. The free surface at the top of the IRWST can be modeled as an adiabatic wall with a zero shear boundary condition. This prevents the modeling of the air-water interaction along the surface.
3. Heat dissipation through the IRWST walls can be ignored.
4. A single pipe is adequate in describing the PRHR.
5. A single phase model can give insightful hints to the behavior of the system.

The fourth assumption is the least valid of the five. A single pipe will not permit any internal flow (i.e flow between the tubes), as would be the case if the actual tube bundle was modeled. The flow will have to bend around the PRHR and not travel through it. The use of a porous media model for this could allow the PRHR to be simulated in a more appropriate manner. However, this approach is not used because it is not compatible with the RPI sub-cooled boiling model. The RPI model uses a wall heat flux partitioning algorithm, and a porous media model does not model walls.

For comparisons between CFX-4.2 calculations and experimental data to be legitimate, a conservation of total heat must be observed. Since the PRHR is being modeled as a single pipe, the surface area is drastically reduced. This brings about an increase in heat flux. This increased heat flux is still within the nucleate boiling region of the boiling curve, so its effects should not alter system behavior drastically.

For this preliminary study a single phase, laminar flow simulation was performed. The IRWST liquid was given an initial temperature of 288 K and an atmospheric initial pressure. The PRHR heat flux is divided into four zones of interest and the prescribed heat flux for these four zones come from the data found in figures 4.2 and 4.4. These heat fluxes are of the order of 10^5 W/m^2. This is well into the nucleate boiling region of the boiling curve, so boiling will occur. Since a single-phase model is being used, the only heat removal mechanism is natural convection. Natural convection removes heat much less effectively than the nucleate boiling mechanism, so by ignoring the nucleate boiling heat transfer, a physically unreal surface temperature will be calculated. In order to prevent this from occurring a "boiling-type" convection coefficient is modeled to remove more heat from the surface of the PRHR, yielding physically real results.

6.1.3 Results and Discussion of Preliminary Model

The preliminary model was developed to offer insight into the physics of the IRWST/PRHR system so that a better final model could be developed. A 15,000 second simulation was performed, which took approximately 7 days and 16 hours of real time. This time was well spent, because numerous observations were made that allowed the geometry to be represented in a simplified manner.

The first effect that was observed was the thermal stratification in the IRWST. This can be attributed to the geometry of the system. The majority of the heat being rejected to the IRWST comes directly from the top section of the PRHR, zone 1. Naturally the heat collects in the upper portion of the IRWST. Figures 6.3 shows the temperature profile throughout the entire elevation of the IRWST at 5,000 and 15,000 seconds. The PRHR is shown on the right side of the figures. The figure also shows that the thermal stratification is predicted by the CFX-4.2 simulation.

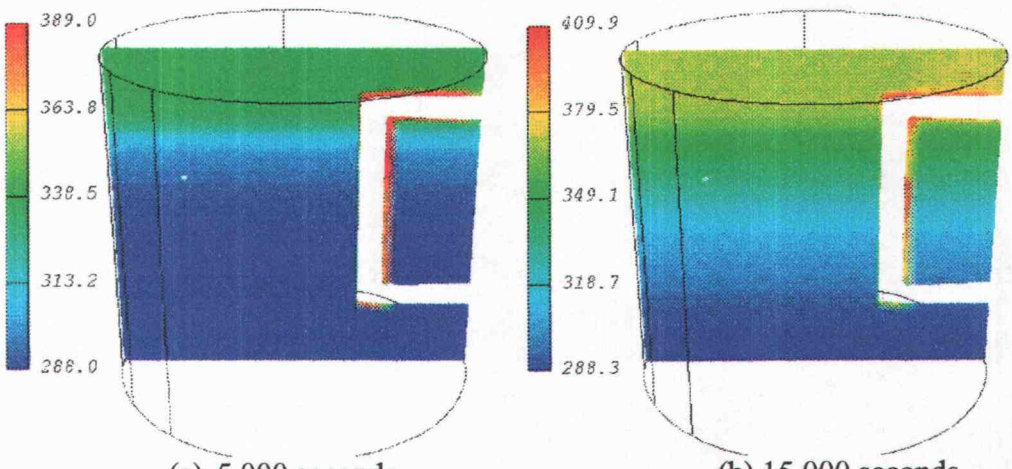

(a) 5,000 seconds (b) 15,000 seconds

Figure 6.3: Temperature (Kelvin) in the IRWST

The next important observation is that the bulk of the IRWST fluid remains virtually motionless (below the top of the PRHR). Figure 6.4 shows the velocity of the fluid at the middle of the tank is nearly zero everywhere. This may be caused by the assumption that the PRHR can be modeled as a single pipe. By modeling the PRHR as a single pipe, all of the adjacent fluid flows upward instead of inward into the center of what should be a tube bundle. This is extremely important because it shows that the single pipe assumption is not valid and the PRHR should be modeled as a few pipes.

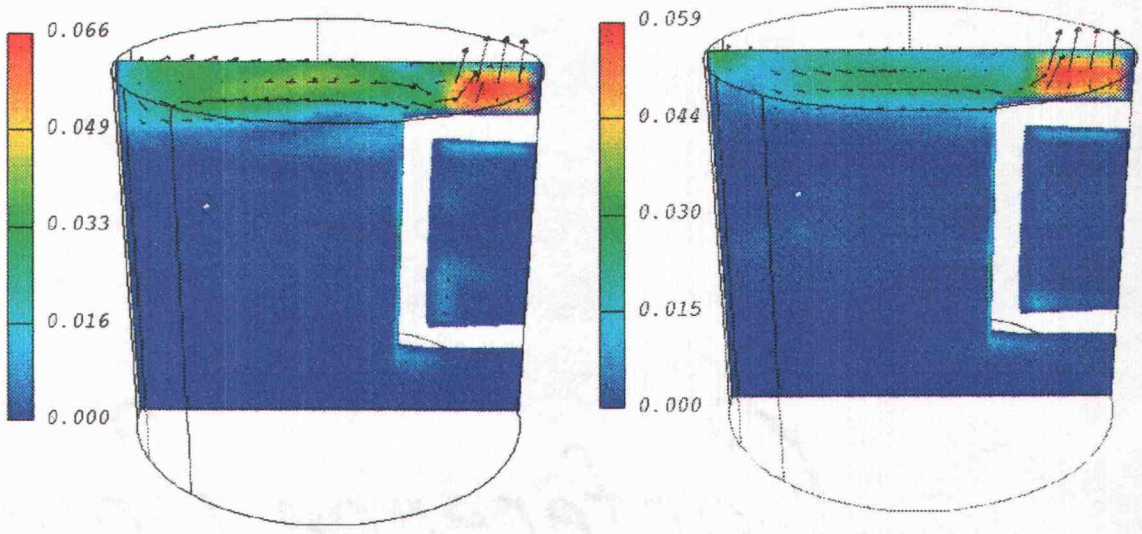

(a) 5,000 seconds (b) 10,000 seconds

Figure 6.4: Velocity (m/s) of the IRWST Fluid at Different Times.

The last and most important observation involves the flow pattern in the upper region of the IRWST, above the top of the PRHR. Figure 6.5 shows the velocity in the x-direction, U, at a distance midway between the top of the tank and the PRHR. The figure shows that the flow pattern is nearly symmetric. This is contrary to what was thought to be observed during the station blackout experiment. There are no physical

measurements within the IRWST during the experiment, only a video of the flow patterns. The interpretation of this video has been openly debated after these calculations were presented for the first time.

An observation that may go unnoticed (but it should not) is the lack of influence of the sparger (white hole) on the flow pattern. This fact led to the most important simplification; the sparger can be taken out of the system with relatively few consequences to the flow pattern. The implication of this allows the PRHR to be modeled as a series of pipes instead of just one, because of the simplified block structure.

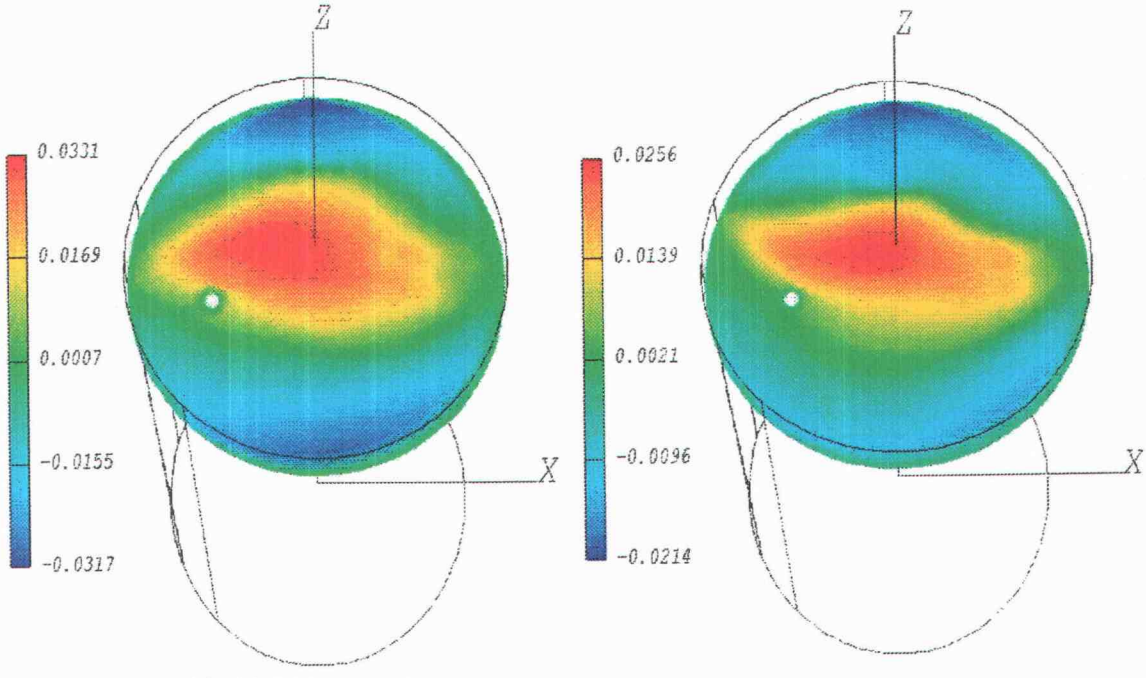

(a) 10,000 seconds (b) 15,000 seconds

Figure 6.5: U-Velocity (m/s) at the Mid-plane between the IRWST and the PRHR

6.2 Final Model

The geometry of the final model is different from the preliminary model in that the sparger is neglected. By neglecting the sparger the number of blocks and cells were decreased, thus allowing a detailed description of the most important component, the PRHR.

The assumptions made are similar to those in the preliminary model with the exception being that the PRHR is not modeled as a single pipe. The flow options, however, have changed in that the simulation incorporates turbulence and sub-cooled boiling models, each of which will be discussed in section 6.2.2.

6.2.1 Geometry and Grid

The absence of the sparger makes the geometry and grid generation simpler. The multi-block method was used and the IRWST was divided into 112 blocks. The block layout is shown in figure 6.6. The figure shows that the block network is a simple arrangement, unlike the preliminary model where the blocks were clustered around the sparger. Without the sparger the IRWST is symmetrical, as is evidenced in the grid.

The grid consists of 44,933 control volumes, most of which are used to resolve the PRHR. A top view of the grid is shown in figure 6.7. A parametric study was conducted which indicated that a grid independent solution was found for a grid this size. The figure shows that the grid is nearly orthogonal and smooth. The only real discontinuity in nodal density is in the area of the PRHR.

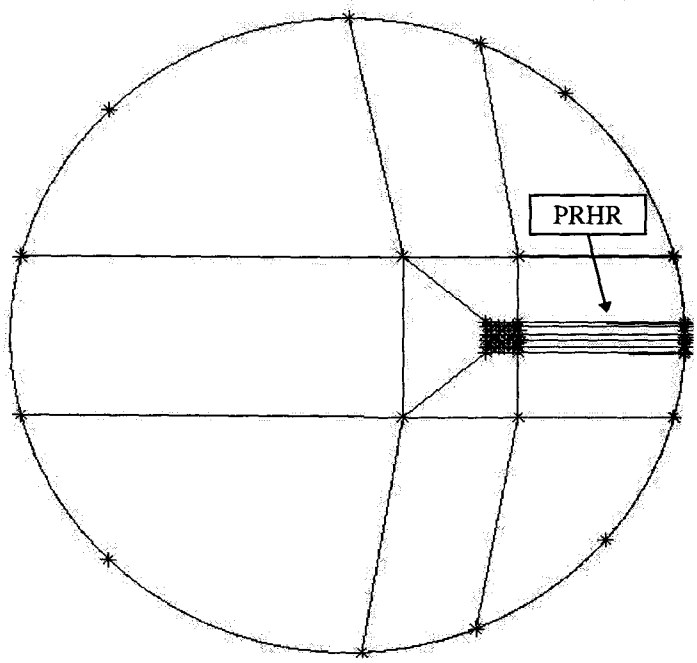

Figure 6.6: Block Network of the Final Model

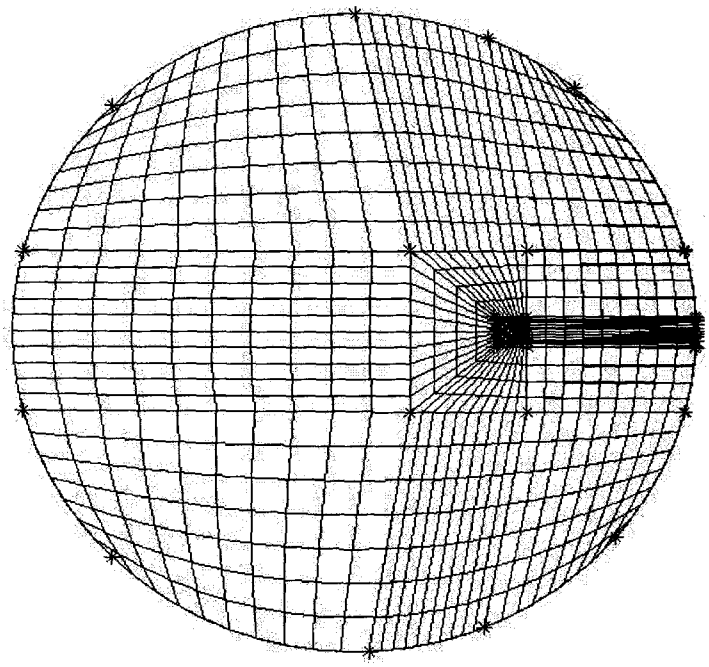

Figure 6.7: Grid for the Final IRWST Model

The PRHR is modeled as four circular pipes. This slightly increases the total surface area, so the PRHR surface heat fluxes are decreased. They are still above the experimental heat fluxes, but the discrepancy is less, so this will yield better results.

The 90 degree bend in the PRHR is difficult to model without drastically affecting the total number of cells and blocks. To compensate for this the top section of the PRHR (zone 1) does not go through a bend, but extends over the vertical section of the PRHR. This is shown in figure 6.8. A similar approach is taken at the bottom of the PRHR, except that the vertical section extends down across from zone 4.

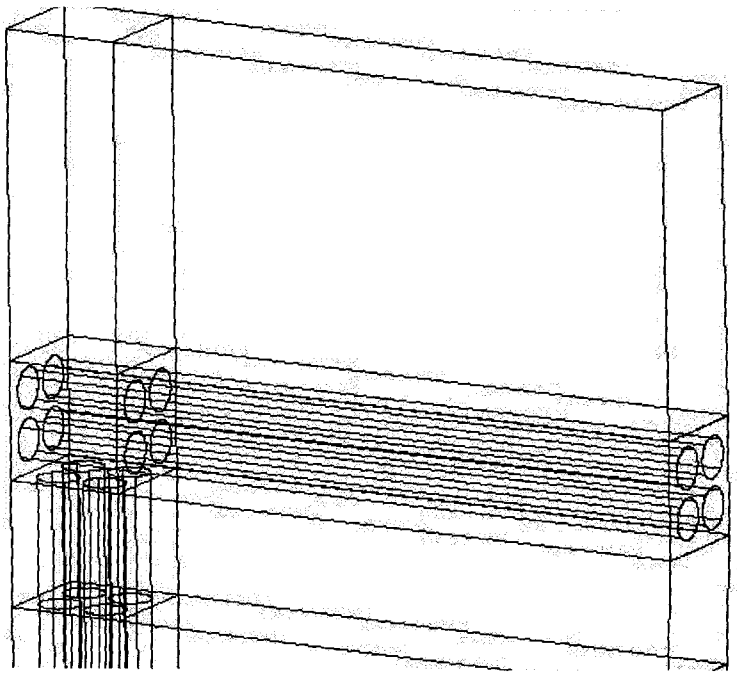

Figure 6.8: Block Network of the PRHR

The above figure also shows that the four pipes are constrained within a box. This is a single-block approach. The reason for using this method is the same as before, memory limitations. A multi-block grid would require 25 blocks to resolve four pipes.

These extra blocks would propagate throughout the geometry dividing each block (of the current geometry) into at least 5 blocks. This would exceed the memory limits, and consequently was abandoned.

The constraint requires that the number of edge sub-divisions be a multiple of five. However, a minimum of two cells between walls is required to calculate the pressure gradient. This places an additional constraint on the grid that requires the total number of subdivisions to be at least 10. The grid wrapped around the PRHR is shown in Figure 6.9.

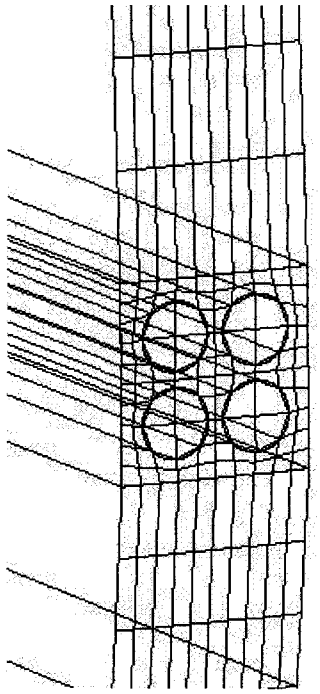

Figure 6.9: PRHR Grid

The aforementioned constraints lead to grid clustering around the PRHR which is excellent because that is the area that requires the highest resolution. However, the

transition from the high cell regions to the low cell regions is not always smooth, so measures have to be taken to improve the smoothness of the grid. The first is the trapezoidal shaped block (shown in Figure 6.6) that helps fan out the constraints on the grid over a larger block. This gives a much better distribution away from the PRHR. This is shown in Figure 6.7. The next measure taken is to impose symmetry of the cell distribution around the PRHR. This alleviates the majority of the smoothness concerns.

6.2.2 Flow Model

The final IRWST model is completed by choosing the flow options that best represent the true physics of the system. These, along with the previously mentioned geometry assumptions, are used to model the flow patterns that develop from the rejection of heat into the IRWST from the PRHR.

The high heat fluxes on the surface of the PRHR are in the nucleate boiling range, so sub-cooled boiling is expected to occur during the early stages of the experiment. The sub-cooled boiling is treated using the RPI model.

The two phases are assumed to be incompressible and the Boussinesq approximation is used to account for buoyancy effects.

The high heat fluxes that are present also make the flow turbulent. The κ–ε turbulence model is used for this simulation. However, since the dispersed phase will only be present in very small quantities during the majority of the simulation, it is a valid approximation to apply the turbulence model only to the continuous phase [25]. Therefore the dispersed phase is modeled with the laminar transport equations. This has

several advantages. First, the required CPU time will be decreased because two fewer turbulent equations need to be solved. It also decreases the amount of user input required in describing the interfacial turbulent transfer terms. When the concentration of the dispersed phase increases both phases should be declared turbulent and the homogenous model for turbulence is suggested. The homogenous model will not require any interfacial transfer terms, so that the only assumption that needs to be applied is the validity of the homogenous model.

The IRWST liquid is initially highly sub-cooled with a temperature of 288 K. This high degree of sub-cooling did not allow to water vapor to leave the surface of the PRHR; it quickly condensed. Knowing this, a study was conducted to test the effect that a single-phase approximation would have on the hydrodynamics of the flow during the early stages of the simulation. A 1,000 second simulation was performed for both a single and two-phase model and the results were identical. The single-phase approximation was carried out until the temperature around the PRHR was 360 K. This occurred at approximately 7,000 seconds.

The PISO pressure correction algorithm [35] is used for all calculations. A parametric study showed that convergent solutions were reached twice as fast with the PISO algorithm than with the SIMPLEC algorithm. [28] The non-linear nature of the transport equations require that the variables be under-relaxed for numerical stability. This is accomplished by multiplying the correction values (calculated by PISO) by a number between zero and one. These numbers are called under-relaxation factors (URF). The URF's are highly dependent upon the type and the properties of the flow, so there is

a high degree of user interaction involved in selecting these values. The selection of URF's effects if the codes ability to produce reasonable results.

False-time stepping is a recommended alternative (by AEA Technology) to under-relaxation for multi-phase flows. This approach is similar to a transient analysis in that it treats each outer iteration of the pressure-correction algorithm as a pseudo-time dependent calculation, see Versteeg *et al* [28] for more information. The main problem with this method is that the user must know the time scale in which the phenomena occurs, so once again there is a certain amount of user interaction that goes into this procedure.

CFX-4.2 does offer a way around the user input, by setting the size of the false time step to the Courant number of the cell. The user can set the false time step size to be any multiple of the Courant number. This method was used often and is very useful in reaching convergent solutions quickly.

6.2.3 Results and Discussion

A simulation of the station blackout experiment was performed for a total of 8,000 seconds; the first 7,000 seconds involved a single-phase approximation. As one would expect the single-phase approximation was much easier to model and takes much less CPU time than the two-phase model. There are two reasons for this; first, the size of the time step can be larger for single phase flow. Second, there are less than half as many equations to be solved. Table 6.1 shows a comparison between the number of time steps, average size of time steps, and run time.

The table shows that the a single-phase simulation could be run with twice the time step size. The single phase model runs 6 times as fast as the two-phase version of the same model. These two facts make the single-phase approximation attractive.

Table 6.1: Comparison between the One and Two Phase Simulations

Number of Phases	Total Time (seconds)	Number of Time Steps	Average Time Step Size (seconds)	Running Time (min.)
1	7,000	1896	3.69	6,791
2	1,000	555	1.80	5,748

One could project that the first 7,000 seconds would require 40,236 minutes (27.9 days) if the two-phase model was used. At this rate a total of 100 days would be required to model the complete 25,000 second experiment.

There are several characteristics of the flow that need to be examined. The most prominent are: thermal stratification, hydrodynamics, counter-current flow, void distribution, and the flow between the PRHR. These will be discussed in the next five sections.

6.2.3.1 Thermal Stratification

The thermal stratification is the most important characteristic of the simulation, because it is the only calculated data that can be compared with experimental data. Figure 6.10 and 6.11 show the thermal stratification predicted by CFX-4.2 at four different times: 1,000, 3,000, 6,000, and 8,000 seconds. The figures clearly show that as

time increases the thermal stratification becomes more appreciable. The reader should note that the scales are different for each figure.

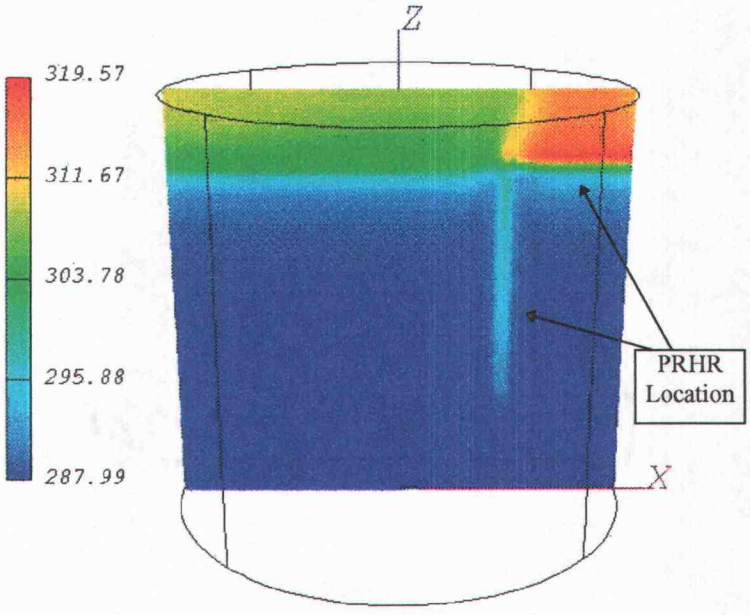

(a) 1,000 seconds

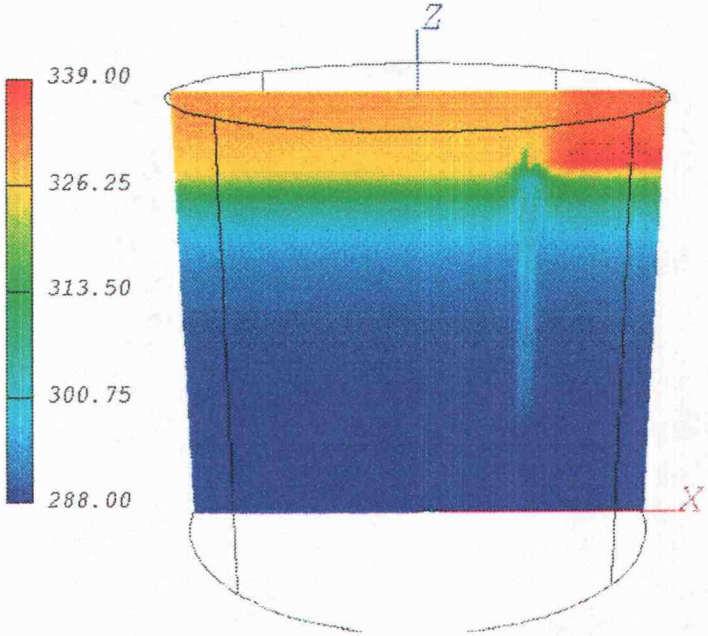

(b) 3,000 seconds

Figure 6.10: Thermal Stratification (Kelvin) in the IRWST

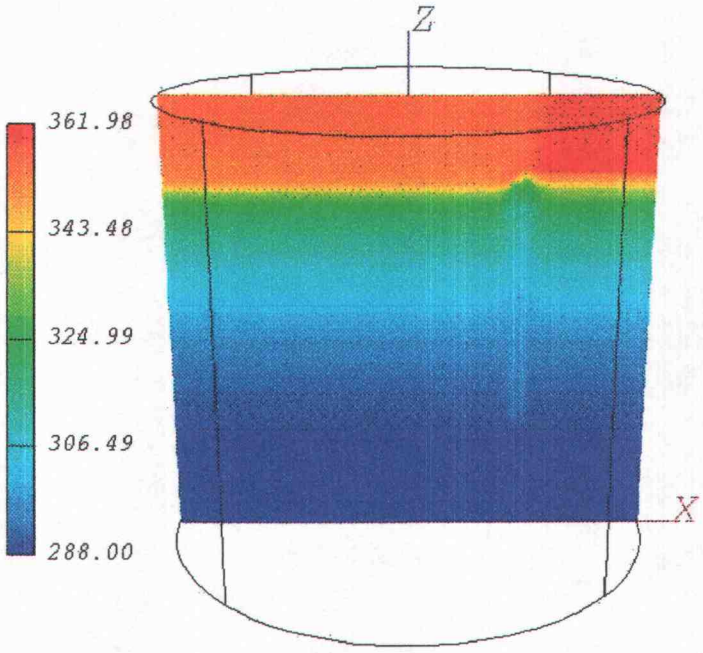

(a) 6,000 seconds

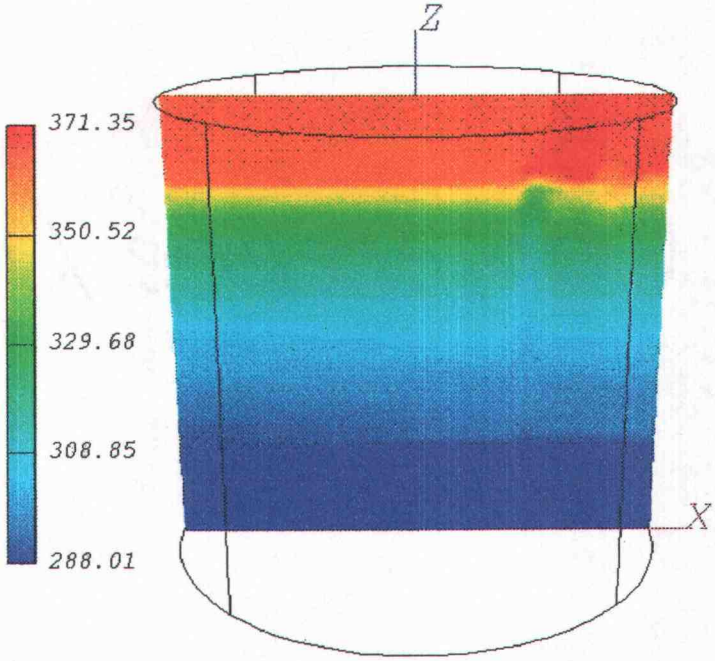

(b) 8,000 seconds

Figure 6.11: Thermal Stratification (Kelvin) in the IRWST (continued)

To compare the CFX-4.2 calculated temperatures with the experimental data, a series of monitoring points were set in the locations of thermocouples TF-703 through TF-709. (refer to Figure 3.6). Figures 6.12 through 6.14 show comparisons between CFX-4.2 and the experimental data for the three thermocouples: TF-709, TF-708, and TF-707.

The figures show that the CFX-4.2 calculation predicts the IRWST temperature reasonably well. The average difference between the experimental data and the CFX-4.2 calculation is 3.19, 2.20, and 0.95 K, respectively. The maximum and minimum difference is 6.37 and 0.64 K respectively. The error associated with the thermocouples is $\pm 2°$ F, which corresponds to a 1.11 K. Clearly, the CFX calculation is within the accuracy for the majority of the data set, but there are sections where it is not. A discussion on the possible cause for the errors is presented in section 6.3.

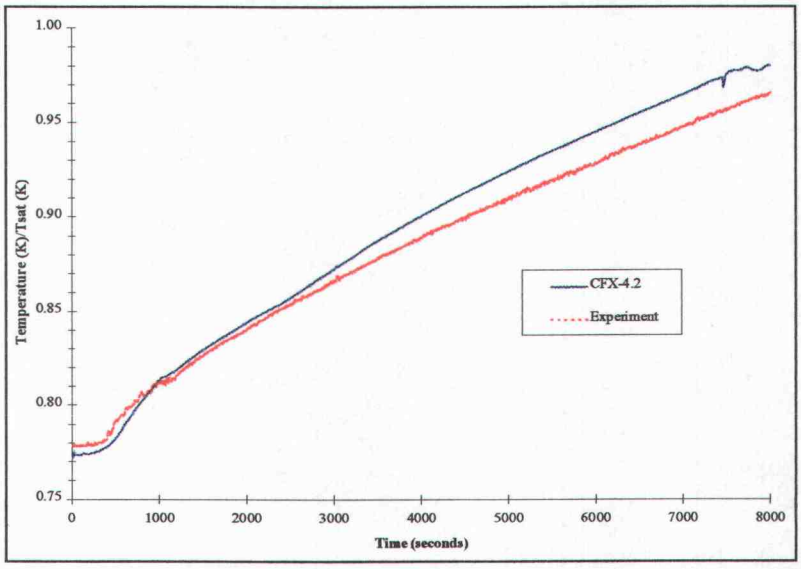

Figure 6.12: Comparison between CFX and Experimental Data for Thermocouple TF-709

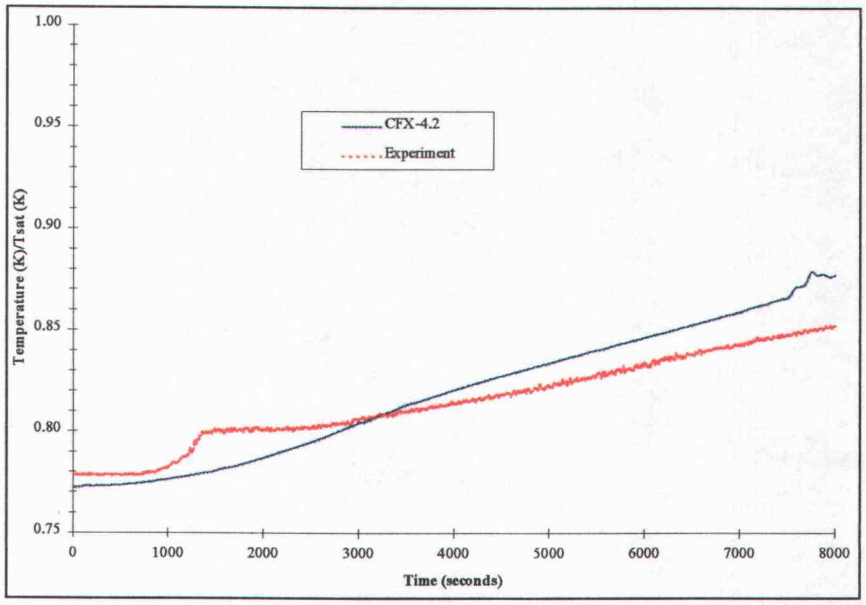

Figure 6.13: Comparison between CFX and Experimental Data for Thermocouple TF-708

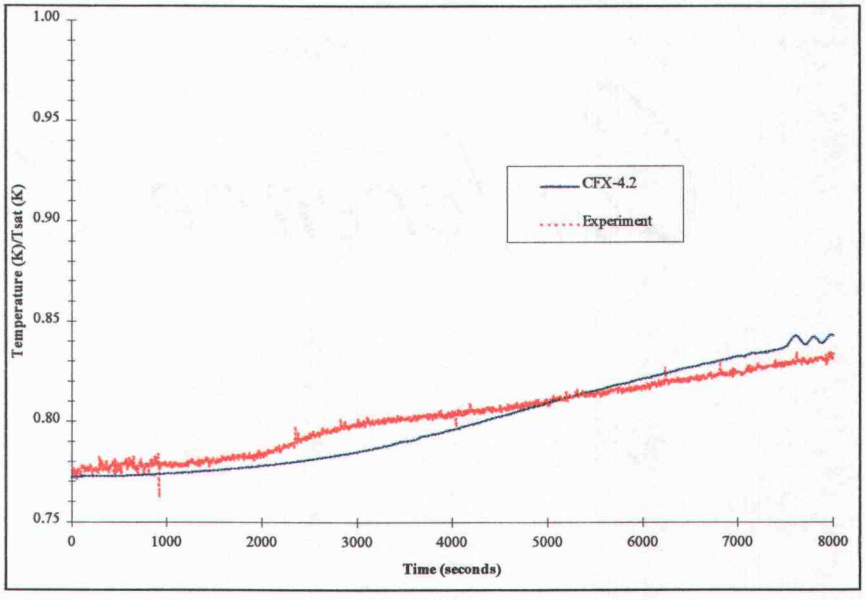

Figure 6.14: Comparison between CFX and Experimental Data for Thermocouple TF-707

6.2.3.2 IRWST Hydrodynamics

This section is devoted to exploring the various IRWST flow patterns. Three flow patterns will be discussed in this section; the circular flow pattern in the top portion of the IRWST, and the upward flow of the water towards the top of the IRWST.

The flow pattern above the IRWST is similar to the pattern presented in the preliminary model section of this chapter. Figure 6.15 and 6.16 show an over-head view of the flow pattern at a position half the distance between the top of the PRHR and the top of the IRWST at 3,000 and 8,000 seconds. The x-direction velocity component, *U*, is represented in the figures, where flow from left-to-right is defined as positive.

The figures show that the flow is nearly symmetric about the x-axis. The heated fluid flows around the tank nearer to the walls and back to the PRHR through the center.

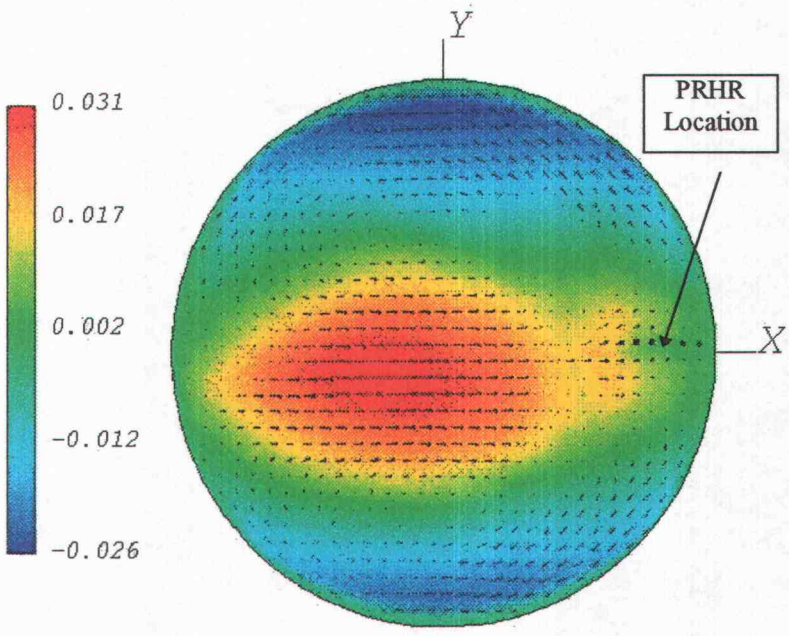

Figure: 6.15: U-Velocity (m/s) above the IRWST at 3,000 seconds

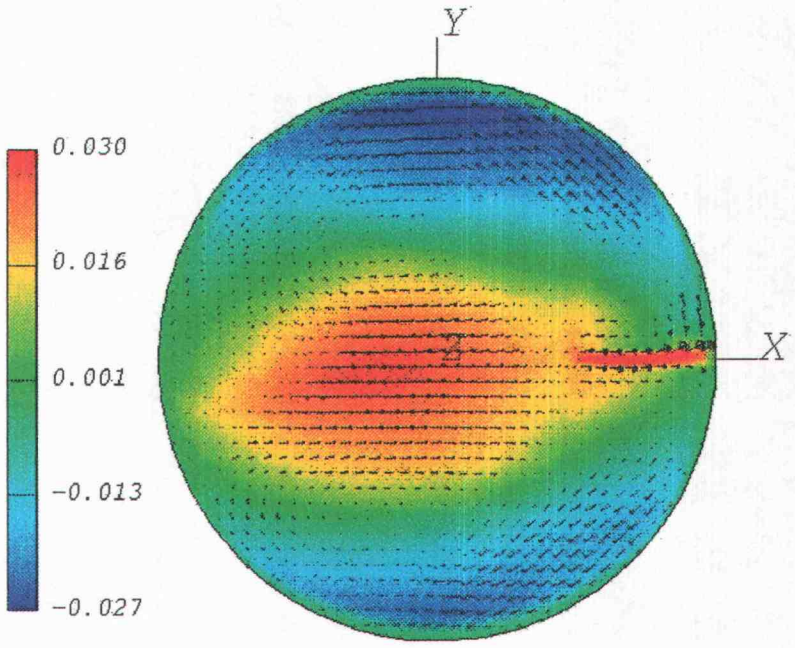

Figure: 6.16: U-Velocity (m/s) above the IRWST at 8,000 seconds

A comparison of the two figures shows that the pattern changes only slightly throughout the experiment.

The next flow of interest is the buoyant flow caused directly by the heating of the fluid by the PRHR. Figures 6.17 and 6.18 show the z-direction velocity component, *W*, at a plane that passes between the PRHR pipes at four different times. The times are 1,000, 3,000, 6000, and 8000 seconds.

The overall flow pattern does not change much over the simulation length. The only noticeable change is the decrease in *W* as the experiment proceeds. This is caused by the decrease in heat input into the system, see Figure 4.2. In Figure 5.18(b) the highest velocity occurs at a lower elevation, which corresponds to an increase in heat flux at zone 3 and a subsequent decrease in the heat flux in zone 1. This explains the decrease in velocity of the plume above the PRHR.

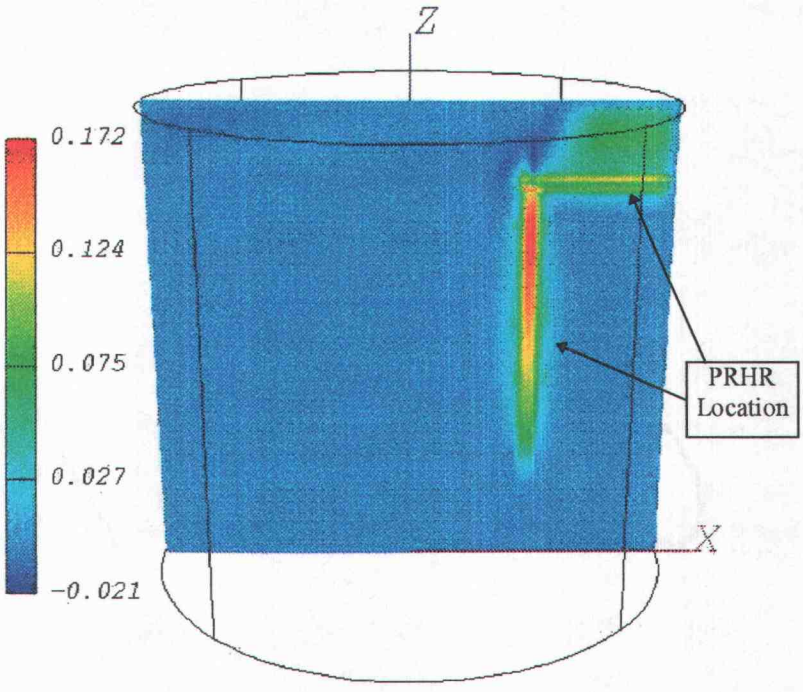

(a) 1,000 seconds

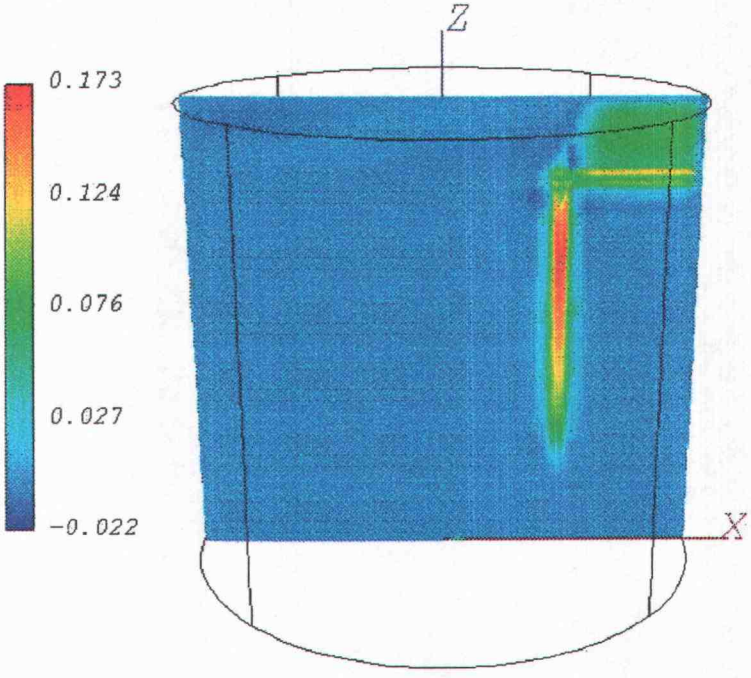

(b) 3,000 seconds

Figure 6.17: W-Velocity (m/s) between the PRHR

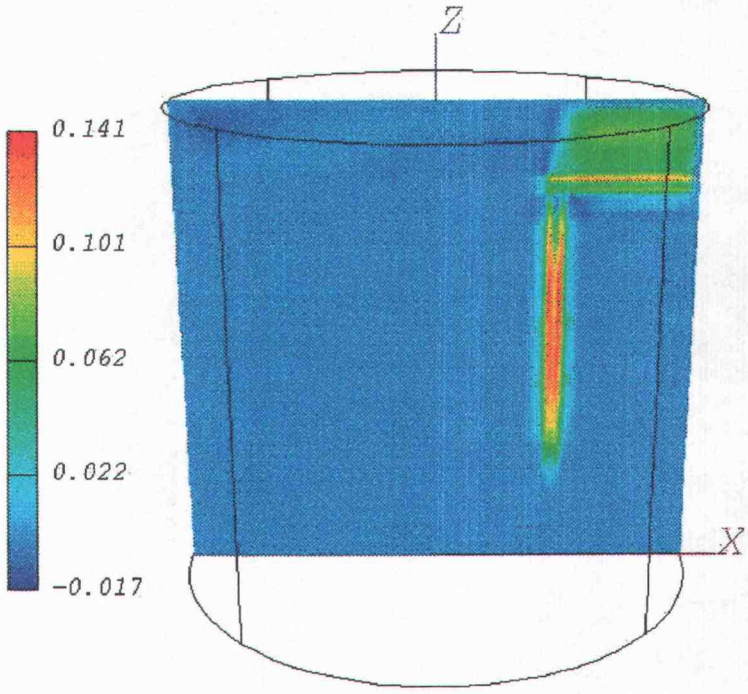

(a) 6,000 seconds

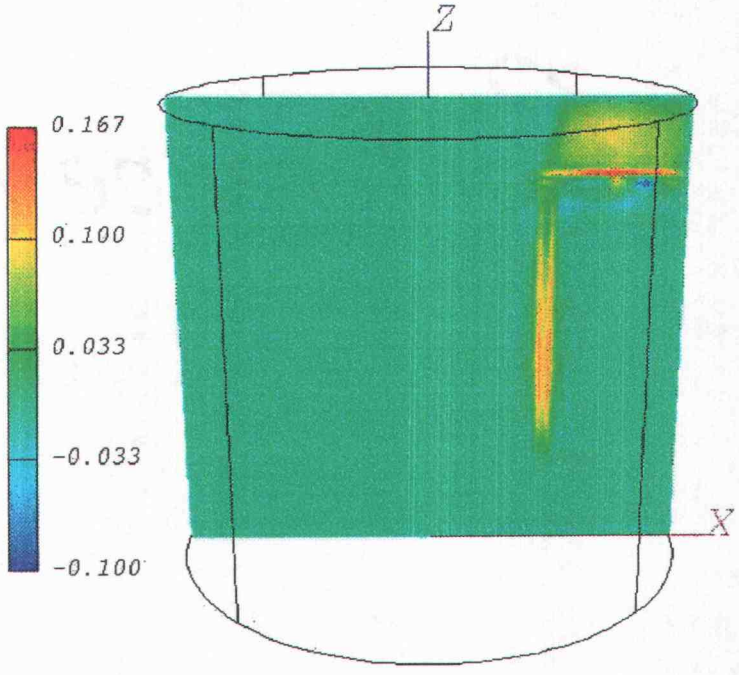

(b) 8,000 seconds

Figure 6.18: W-Velocity (m/s) between the PRHR (continued)

The final flow pattern that needs to be mentioned is the flow below the top of the PRHR. Figures 6.17 and 6.18 show that the *W*-component of the velocity is nearly equal to zero away from the PRHR in the bottom portion of the IRWST. However, this does not prove that there is no significant flow field in those areas because the flow may only be occurring in the x and y-directions. Figure 6.19 shows the magnitude of the fluid's velocity (speed) at 8,000 seconds. As the figure shows there is only slight fluid motion below the PRHR. The most interesting aspect of the figure is the relative motion occurring above the PRHR. As the tank is transversed from top to bottom, the flow is initially 0.03 m/s (approximately). It then slows to practically zero and then increases in speed again. This relative motion will increase heat transfer and shows that it is possible that a counter-current flow may be occurring. If this is occurring then it will further increase the heat transfer through the tank.

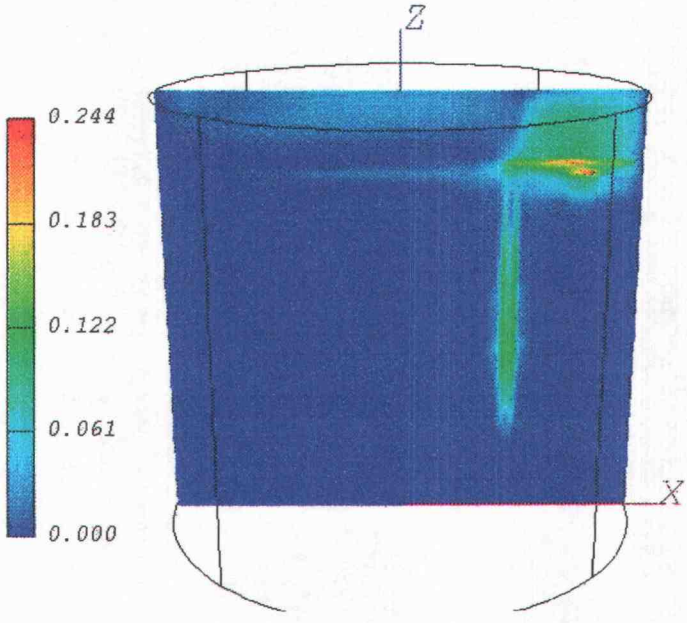

Figure 6.19: Overall Speed (m/s) of the IRWST Water at 8,000 seconds

6.2.3.3 Counter-Current Flow

Figure 6.19 suggests that there may be counter-current flow occurring in the region of the IRWST above the PRHR. This is an important effect because it will increase the amount of heat being transferred through the thermal layer interface into the lower portions of the IRWST. Since the buoyant flow will carry the majority of the heat into the top of the IRWST, an efficient way to re-distribute that heat throughout the tank is needed. A counter-current flow between the interface will help do just that. In order to support the claim of a counter-current flow situation two different plots will be presented, each at two different times.

The first plot is similar to the one shown in figure 6.19, but the variable plotted is *U*. The times used are 5,000 and 8,000 seconds and the plots are shown in Figure 6.20. The figure shows that there is slight counter-current flow at the elevation directly below the PRHR. There also appears to be a small layer of stagnant fluid above the PRHR.

Figure 6.21 shows the IRWST from a different angle. The IRWST is rotated 90° so that the slice will transverse the PRHR pipes. These two plots show the y-direction velocity component, *V*, where a positive *V* flow is defined to be from left to right. This figure supports the claim of a counter-current flow.

Figure 6.21 also shows that the flow pattern is just a simple re-circulation pattern similar to that of a vertical heated wall. The solution to the vertical heated wall problem never accounts for the effect of an upper boundary because it is assumed to be far away. This shows that modeling of the free surface is not very important hydrodynamically since it far away.

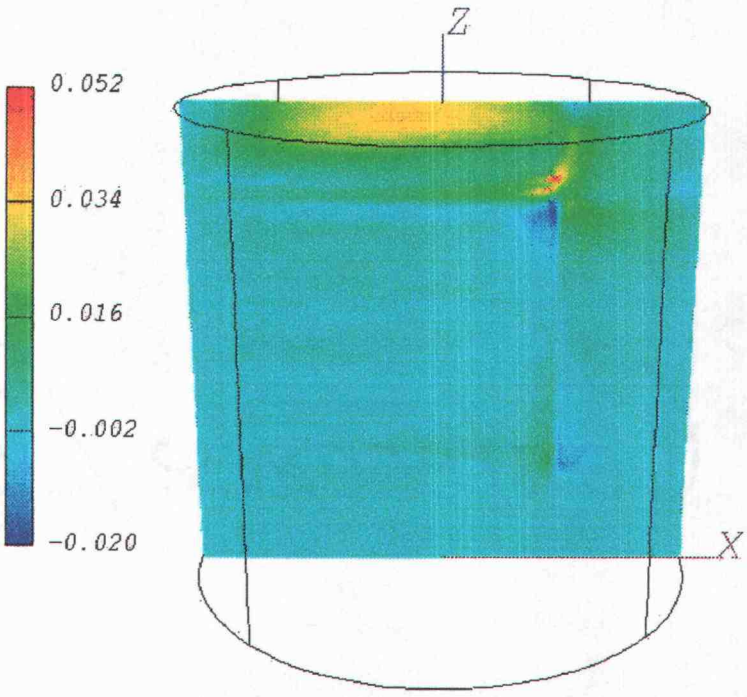

(a) 5,000 seconds

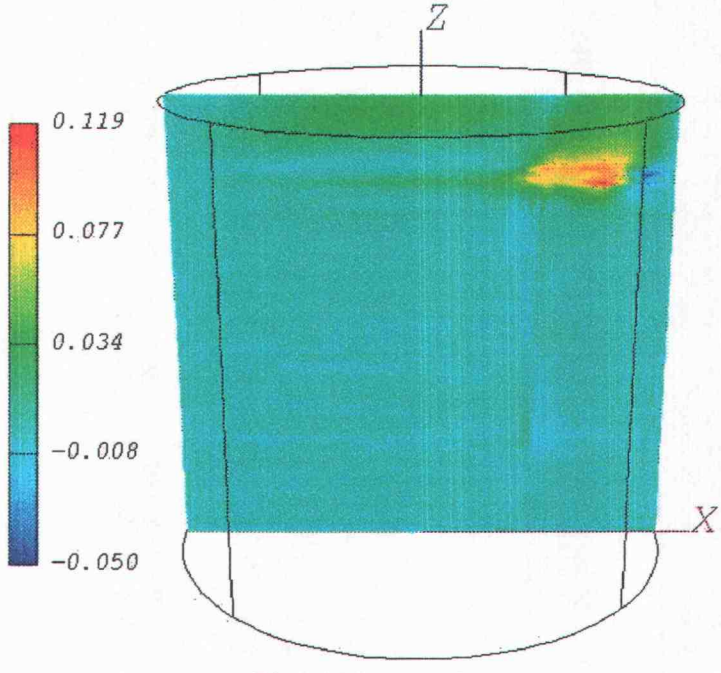

(b) 8,000 seconds

Figure 6.20: *U*-Velocity (m/s) between the PRHR

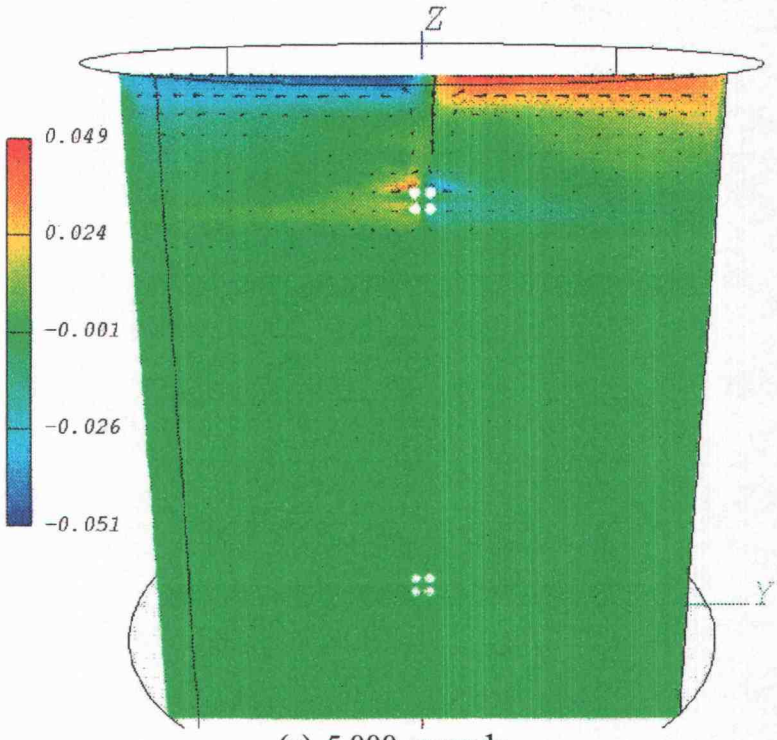

(a) 5,000 seconds

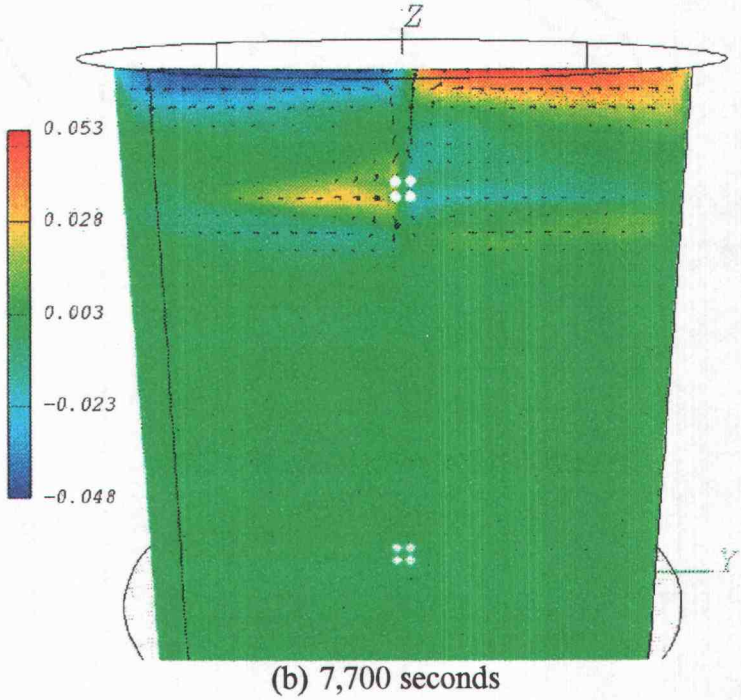

(b) 7,700 seconds

Figure 6.21: *V*-Velocity (m/s) around the PRHR

6.2.3.4 Void Distribution

The void fraction (volume fraction of steam) is only significant around the PRHR, since the water is sub-cooled. The following figures show the void fraction in three positions. Figure 6.22 shows the void fraction around zone 1. Figure 6.23 shows the void fraction at the PRHR for all four zones, and Figure 6.24 shows an over-head view of the void fraction at an elevation level that encompasses zone 2.

Figure 6.22 shows the void fraction with the surrounding water 5 K sub-cooled. The figure shows that the steam does not travel far into the liquid continuum before it condenses.

Figure 6.23 shows that the only location that has a significant amount of void is around zone 1 of the PRHR. Figure 6.24 shows that there is a small amount of vapor around zone 2, but since the surrounding fluid is 20 K sub-cooled it never leaves the surface of the wall.

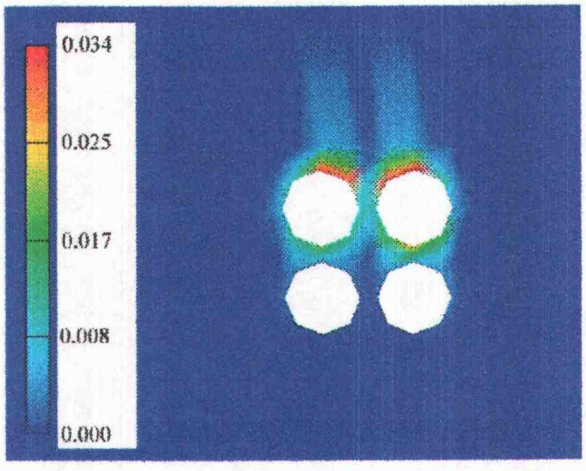

Figure 6.22: Void Fraction around Zone 1 of the PRHR
with 5 K of sub-cooling.

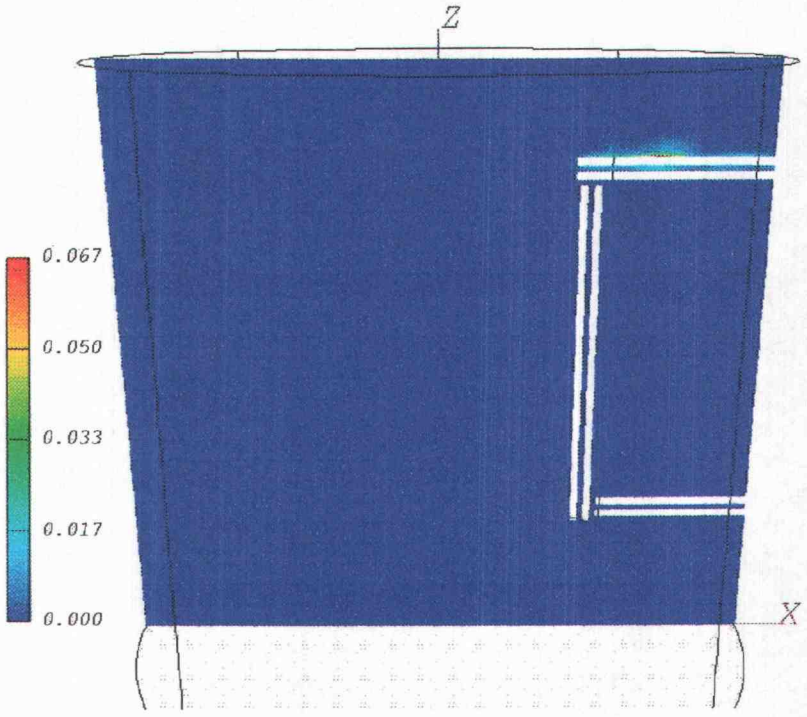

Figure 6.23: Void Fraction around the PRHR
with 5 K sub-cooling

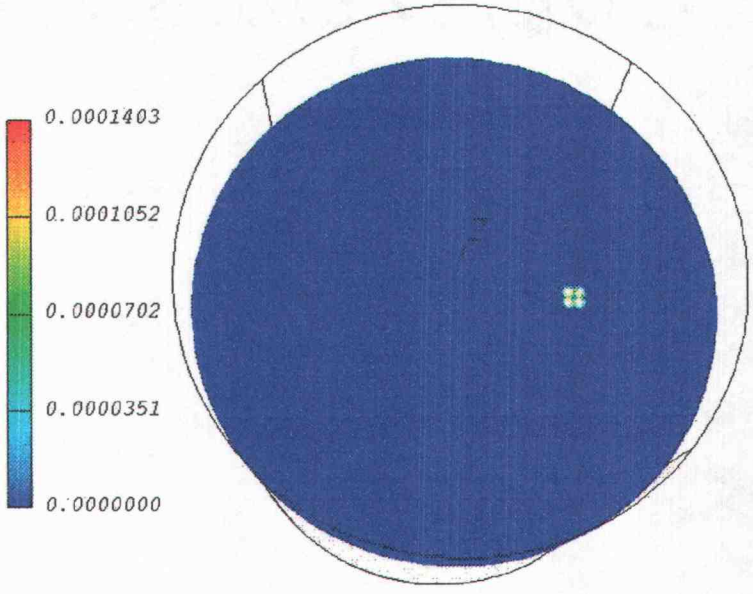

Figure 6.24: Void Fraction around Zone 2 of the PRHR
with 5 K sub-cooling

6.2.3.5 PRHR Between Flow

The PRHR was modeled as four pipes so that a fluid(or fluids) could flow between the bundle in a similar manner as would occur through the actual PRHR in the APEX test facility. Since the flow is driven by buoyant forces, the dominant flow will be in the direction of gravity, which is the z-direction in this model. Figures 6.17 and 6.18 showed the *W*-velocity at the mid-plane between the PRHR, but did not show how the flow circulates around and between the PRHR.

Figure 6.25 shows the *W*-velocity of liquid water around through the PRHR at 8,000 seconds. The liquid is at its fastest between the top two pipes when it reaches 0.182m/s . This is approximately twice the speed of the liquid on theouter surfaces of the PRHR. The increased speed helps remove the heat more effectively than the single pipe model. The added benefit is that the multi-pipe model compares better with experimental data than the single-pipe model.

There is water vapor present around zone 1 of the PRHR, and there is significant flow of the vapor around the PRHR. Figure 6.26 shows the vapor flow in the z-direction, *W*. This figure shows that the steam flow reaches approximately half the distance to the top of the IRWST. The vapor reaches a maximum *W*-velocity of 0.393 m/s between the pipes. This is three times the speed of the liquid. Since the steam is less dense this is exactly what is expected. It is also reassuring that there is no flow in the negative z-direction.

The void fraction shown in figure 6.22 shows that the vapor is present in small quantities. However, it is still transferring mass, momentum and heat to the liquid phase,

so it will have an impact on the flow. However slight the impact may be with this level of concentration, it still should be considered.

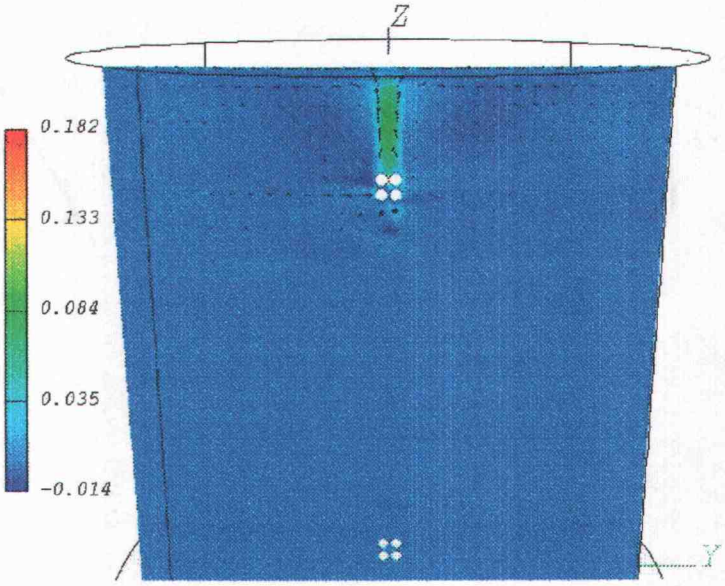

Figure 6.25: Liquid *W*-velocity (m/s) Through the PRHR

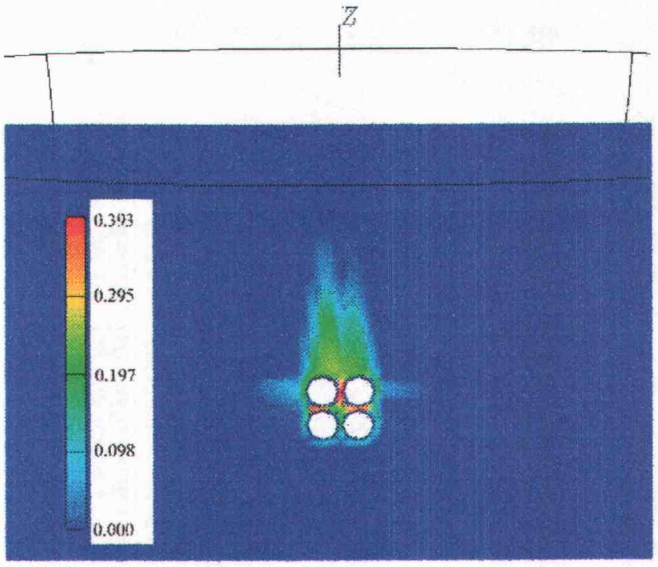

Figure 6.26: Vapor *W*-velocity (m/s) Through the PRHR

6.3 Sources of Error

The numerical solution is affected by many factors that introduce error into the final result. When using numerical analysis there are obvious errors associated with the differencing schemes employed, such as truncation error and numerical diffusion and dispersion. In addition to these errors, there are errors associated with the quality of the grid that occur when transforming the solution to the body-fitted coordinate system from the computational coordinate system. Another source of error is the assumptions that were made in the description of the geometry. These three sources of error will be briefly discussed in the remainder of this section.

6.3.1 Numerical Errors

These errors are associated with the numerical algorithm(s) being employed. The first, and most obvious, is the truncation error associated with the particular differencing scheme used. All of the equations are discretised with the hybrid differencing scheme [25], with the exception of the pressure, volume fraction and density equations. The pressure equation uses central differencing and the density and volume fraction equations use the upwind scheme.

The hybrid scheme is a combination of the central and upwind methods. The choice of method depends upon the Peclet number at the cell faces. When the absolute value of the Peclet number is less than two, central differencing is used, otherwise the upwind method is used. The two schemes, when applied to the time-dependent convection-diffusion equation, are second order accurate in space and first order accurate

in time [34]. The size of the control volumes should be as small as possible to prevent large truncation errors. The average control volume size for the IRWST model is small enough to prevent large truncation errors occuring. However, the grid size was changed until the calculated solutions failed to change significantly, so the truncation error is at the smallest reasonably achievable value.

Inherent in these two schemes are numerical diffusion and dispersion. These effects arise from the behavior of the truncation terms in the finite difference equations. Numerical diffusion tends to smear out sharp gradients and dispersion can produce small oscillations in the solution. These errors in this incompressible simulation are not likely as large as one might see in a compressible flow simulation, because of the absence of strong discontinuities in the solution.

A large portion of the errors are associated with the non-linearity of the transport equations. The stability of the solutions for these equations is highly dependent upon the under-relaxation factors and to a lesser extent the velocity-pressure coupling algorithm. The PISO algorithm by Issa [35] was used for this model. PISO is designed to be semi-implicit non-iterative method. Issa showed that the PISO algorithm has a fourth order error term when the velocity-pressure coupling is not iterated on. This is two to three orders smaller than the error associated with the time differencing methods, so it is not considered to be significant. However, experience shows that it is wise to iterate on complex systems with complex boundary conditions.

When solving such a large number of equations it is difficult to check each variable for convergence. This especially true for the IRWST model, because there is no

inlet or outlet for the flow. Generally, one would calculate the mass residuals (net mass into a cell) and continue to iterate until the mass residual was equal to or less than a set number, usually 0.1% of the total inlet mass flow. Since, there is no inlet flow it is difficult to judge if convergence was reached. For this situation, it is suggested that CFX-4.2 calculate the residual to the fullest extent that the machine will allow, so the transport equations should be iterated until nothing changes. Then the solution is considered converged. This can be difficult to do when fifteen variables are considered, so it is possible that certain variables may not be fully converged. Convergence failure is the most likely source of significant error involved with the numerical schemes employed in this work.

6.3.2 Geometry Errors

The errors commonly associated with body-fitted coordinate systems all apply here. The most common of these are found with non-orthogonal grids. For these grids, an accurate transformation from computational space to physical space is often difficult. Another common error concerns steep changes in cell density, which will also make transformations difficult, and can effect the value of the calculated gradients in that area. The last common error is associated with the size of the control volume. Large control volumes decrease the accuracy of the solution and should be avoided whenever possible.

6.3.3 Assumptions and Choice of Models

In this research, turbulent two-phase flow was modeled. There are many possible sources of error in this type of modeling. The current turbulent two-phase models are not well developed and tested. Their accuracy can only be estimated and great caution should be exercised when employing them.

The κ–ε turbulence model has been found to work poorly with some recirculation flows, similar to the one seen here [28], so there is some additional error here.

The approximation of the free surface as a zero-shear adiabatic wall will introduce error into the calculation. First, in a hydrodynamic sense their are errors involved by not modeling the air/water interface. Secondly, by ignoring the free surface no heat escapes the system. No heat loss to the surrounding will lead to the higher temperatures within the IRWST.

In order to illustrate the effects of not accounting for heat losses, a simple analysis can be performed. An energy balance is performed around the portion of the IRWST above the PRHR, assuming that only the heat rejected by zone 1 enters the volume and that heat is allowed to leave through natural convection off the free surface and the sides of the IRWST, as shown in figure 6.27. The water in the IRWST and the surrounding air are initially in thermal equilibrium. The temperature distribution with the IRWST is assumed to be homogenous, and conduction through the IRWST wall is ignored.

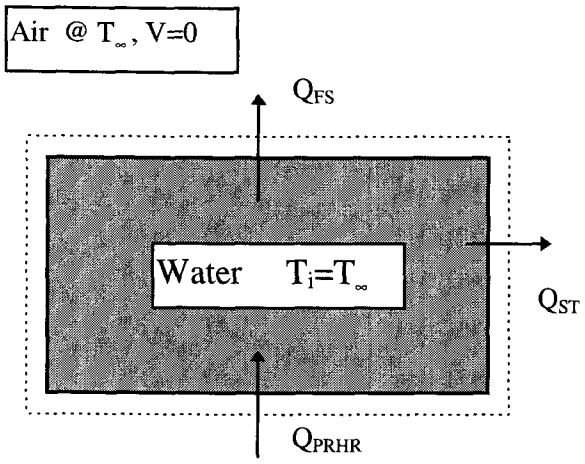

Figure 6.27: Energy Control Volume

The energy balance around the control volume in Figure 6.27 is written as

$$mc_p \frac{dT}{dt} = \overline{Q}_{PRHR} - (hA)_{FS}(T - T_\infty) - (hA)_{TS}(T - T_\infty) \tag{6.1}$$

or in terms of temperature rise, $\theta = (T\text{-}T_\infty)$.

$$mc_p \frac{d\theta}{dt} = \overline{Q}_{PRHR} - \{(hA)_{FS} + (hA)_{TS}\}\theta \tag{6.2}$$

The first term on the R.H.S. of equation (6.2) is the average heat being input by zone 1 of the PRHR.

The temperature rise in the IRWST with losses is shown below

$$\theta^W = \frac{\overline{Q}_{PRHR}}{(hA)_{eff}}\left(1 - \exp\left(-\frac{(hA)_{eff}}{mc_p}t\right)\right)$$

$$where \tag{6.3}$$

$$(hA)_{eff} = (hA)_{FS} + (hA)_{TS}$$

The temperature rise without losses is found by setting $(hA)_{eff}$ to zero in equation (6.2), and is given by

$$\theta^{W/o} = \frac{\overline{Q}_{PRHR}}{mc_p} t \tag{6.4}$$

The error associated with neglecting heat losses is found by subtracting equation (6.3) from equation (6.4). The total error at 8,000 seconds was found to be 2.5 K, equation (6.5). This is a conservative estimate because it assumed that the only heat entering the control volume was from zone 1, when in reality a large portion of the heat from zones 2 and 3 also enters the top portion of the PRHR. Including these would certainly increase the predicted temperature rise.

$$\theta^{W/o} - \theta^{W} \cong 2.5K \tag{6.5}$$

The inability to model all of the tubes in PRHR also introduces errors into the system. The high heat flux will increase the localized temperature, thus increasing the buoyant force and the speed of the flow. This can also effect the boiling model's ability to predict the phenomena properly if the elevated heat flux is out of the range of application for the model. Fortunately this was not the case in this work.

Chapter 7. Conclusions and Future Work

CFX-4.2 was used to model the flow patterns within the IRWST of the OSU APEX thermal-hydraulic test facility. The model included a single-phase approximation during the highly sub-cooled portions of the test and a two-phase model to account for sub-cooled boiling once the temperature reached 360 K. The simulation was conducted over a 8,000 seconds interval. The first 7,000 seconds used a single-phase approximation. Several conclusions can be drawn with regard to this research, the majority of which involve results of the CFX-4.2 model, but several involve the application of CFD techniques to model the various systems found in nuclear plants is also evaluated.

The model was able to predict the thermal stratification found within the IRWST during the station blackout experiment. A comparison between experimental data was found to be within 6 K of the CFX-4.2 calculated values.

It was also found that below the top section of the PRHR, the bulk of the IRWST fluid is virtually motionless, while the flow above the PRHR is re-circulating symmetrically around the PRHR, contrary to the circular flow pattern thought to be observed during the experiment.

CFX-4.2 successfully modeled the flow around four pipes that were used to model the PRHR. When flowing through zone 1 of the PRHR the liquid velocity reached approximately 0.182 m/s, while the vapor velocity reached velocities of 0.393 m/s. The vapor travels at a faster speed than the liquid, as one would expect.

The void distribution was only observed around zone 1 of the PRHR. Steam was present in small quantities with a maximum void fraction of 0.034. The voiding region extended approximately half the distance to the top of the IRWST where all voids completely condensed.

Several conclusions can be drawn about the usefulness of applying commercial CFD software to nuclear related applications. This research showed that CFD codes are capable of modeling a great deal of flows that involve several different phenomena. However, it is not without a heavy price. The modeling of two-phase flows, in particular of boiling systems, is very difficult and time consuming. Two-phase flow modeling is extremely sensitive to under-relaxation factors or the false-time step size and as the system changed it became necessary to vary these to avoid instabilities in the solution. This model encompassed a wide variety of flows and thermal conditions so these parameters changed often throughout the experiment making it extremely difficult to generate consistently good results. The difficulty is that there is no way to know when the under-relaxation parameters need to be changed until the instabilities actually arise. This caused a lot of lost time in modeling the system. The 4.0 days that it took to model the 1,000 second two-phase interval was probably closer to one full week because of the lost time.

With increasing CPU speed, the modeling of two-phase systems will become easier and less time consuming. Presently, the time required to model the two-phase boiling system is prohibitive. The modeling of two-phase boiling should be restricted to systems smaller than the IRWST and to shorter transients. The size of the IRWST was not as large a problem as the duration length of the experiment.

Finally, the necessity of modeling the boiling on the PRHR is also questioned. The single-phase approximation yielded the same flow patterns and to some extent predicted the temperature distribution more accurately. However, this is in all probability an isolated situation where the boiling heat transfer and hydrodynamics did not dominate the system. This would not be so for smaller systems, such as fuel assemblies and pressurizers etc.

Commercial codes such as CFX-4.2 should never be thought of as a black box that gives an answer. Numerous specialty codes like TRAC and RELAP can be treated like this, because the user can run a simulation without the trouble of finding convergent solutions and setting under-relaxation factors. The user of a CFD code, must have or develop a strong understanding of the numerical algorithms used to solve the transport equation to make the best use of the code. The applications of CFD to the power industry should receive more attention in the future. Despite the current short-comings, CFD is still a very powerful tool that deserves further development and study.

Some future work should be performed with this model. One study that could be performed is declaring the velocity components of the liquid to be quasi-static, since the flow did not vary drastically throughout the simulation. This means that they would be assumed to have reached a steady state. This would speed up the simulation but would introduce another possible cause of error.

The size of the time step during the two-phase simulation was 2 seconds. This is probably too large to resolve all the phenomena that are occurring and did introduce error into the system. Time steps of 0.1 or 0.5 seconds would be ideal and the

effects of using smaller time steps should be explored when the CPU speeds allow for a faster simulation. The smaller time steps will also yield better comparisons with the experimental data.

Bibliography

1. Ishii, M. (1975), *Thermo-fluid Dynamic of Two-Phase Flows,* Eyrolles, France.

2. Kurul, N (1990), *Multifimensional Effects in Two-Phase Flow including Phase Change*, PhD Thesis, Rensselaer Polytechnic Institute

3. TRAC-PF1/Mod 2 Code Manual (1993), Nuclear Technology and Engineering Division, Los Alamos National Laboratory, Los Alamos, New Mexico.

4. RELAP5/MOD3.2 Code Manual (1995), Idaho National Engineering Laboratory, Idaho Falls, Idaho.

5. Drew, D. and R.T. Lahey Jr. (1979), *Applications of General Constitutive Principles to the Derivation of Multidimensional Two-Phase Flow Equations*, International Journal of Multiphase Flows, Vol. 5 pp243-264.

6. Ishii, M and K. Mishima (1981), *Study of Two-fluid Model and Interfacial Area*, ANL-80-111

7. DelValle, M. and D.B.R Kenning (1985), *Subcooled Flow Boiling at High Heat Flux*, International Journal of Heat and Mass Transfer, Vol 28 pp 1907-1920.

8. Wolfert, K., M.J. Burwell and D. Enix (1978), *Non-Equilibrium Mass Transfer Between Liquid and Vapour Phases During Depressurization Process in Transient Two-Phase Flow*, Proc. 2nd CSNI Specialists Meeting, Paris, France, pp 1377-1387.

9. Kurul, N, M. Podowski, H. Anglart and O. Nylund (1995), *CFD Prediction of Flow and Phase Distribution in Fuel Assemblies with Spacers,* 7th international Meeting on Nuclear Thermal-Hydraulics (NURETH 7), Saratoga Springs, NY, Sep. 10-15, 1995.

10. Kurul, N. And M. Podowski (1990), *Multidimensional Effects in Forced Convection subcooled Boiling*, 9th International Heat Transfer Conference, Jerusalem, Israel, August 1990.

11. Drew D., L. Cheng and R.T. Lahey Jr. (1979), *The Analysis of Virtual Mass effects in Two-Phase Flow,* International Journal of Multiphase Flow, Vol. 5 pp 233-242.

12. Watanabe T., M.Hirano, F. Tanabe and H. Kamo (1990), *The Effect of the Virtual Mass Forece term on the Numerical Stability and Effeciency of System* Calculations. Nuclear Engineering and Design, **120**(1990) 181-192.

13. Saha, P. And N. Zuber (1974), *Point of Net Vapor Generation and Vapor Void Fraction in Subcooled Boiling,* Proc. 5th International Heat and Mass Transfer Conference, Tokyo, Japan.

14. Lahey, R.T. (1978), *A Mechanistic Subcooled Boiling Model,* Proc, of the 6th International Heat Transfer Conference, Toronto Canada, Vol. 1 pp 293-297.

15. Yuan, Z. And E.E. Michaelides (1992), *Turbulence Modulation in Particulate Flows-A Theoretical Approach,* International Journal of Multiphase Flows, Vol 5, pp 779-785.

16. de Bertodano, Martin and Anis A. Saif (1996), *Modified* κ–ε *model for Two-Phase Turbulent Jets*, Proc. of the Japan-U.S. Seminar on Two-Phase Flow Dynamics, Fukuoka, Japan, July 15-20 1996.

17. de Bertodano, M.L., R.T Lahey Jr. and O.C. Jones (1994), *Development of a* κ–ε *model for bubbly two-phase flow*, Journal of Fluids Engineering, **116**:128-134

18. Sato, Y., M. Sadatomi and K. Sekoguchi (1981), *Momentum and Heat Transfer in Two-Phase Bubble Flow-I and II,* International Journal of Multiphase Flow, Vol. 7, 167-177 1981.

19. Groome, J.T., J.N. Reyes, A.Y. Lafi, O.L. Stevens (1996), *Quick Look Report for the OSU APEX NRC-2, Station Blackout with Modified ADS logic*, APEX Long-Term Cooling Test Facility, Department of Nuclear Engineering, Oregon State University, Corvallis, Oregon. November 1996.

20. Stevens, Owen L., (1996), *Characterization of the Advanced Plant Experiment (APEX) Passive Residual Heat Removal System Heat Exchanger,* M.S. Thesis, Oregon State University.

21. Aya, Izuo, Hideki Nariai (1991), *Evaluation of Heat-Transfer Coefficient at Direct Contact Condensation of Cold Water and Steam.* Nuclear Engineering and Design 131(1991) 17-24.

22. Thomas, R.M. (1979), *Condensation of Steam on Water n Turbulent Motion,* International Journal of Multiphase Flow **5**(1979) p 1-15

23. Murata Akira, Eiji Hihara, Takamoto Saito (1992), *Prediction of heat transfer by direct condensation at a steam-subcooled water interface*, International Journal of Heat and Mass Transfer **35** p 101-109.

24. Anderson, Dale A., Richard H. Pletcher, and John C. Tannehill (1997), *Computational Fluid Mechanics and Heat Transfer 2nd edition*, Taylor and Francis, Washington D.C.

25. CFX-4.2 Solver Manual (1997), AEA Technology. CFX international, 8.19 Harwell, Didcot, Oxfordshire OX11 0RA, United Kingdom.

26. Bejan, Andrian (1995), *Convection Heat Transfer 2nd edition*, John Wiley and Sons, Inc., 605 Third Avenue, New York, NY 10158-0012.

27. Launder, B.E. and B.T. Sharma (1974), *Applications of the energy dissipation model of turbulence to the calculation of flow near a spinning disc*, Lectures of Heat and Mass Transfer 1, 131-138

28. Versteeg, H.K., and W. Malalasekera (1995), *An Introduction to Computational Fluid Dynamics-The Finite Volume Method*, Longman Scientific and Technical, Essex CM20 2JE,England

29. Schiller, L., and A. Naumann (1933), VDI Zeits., volume 77 p318.

30. Ishii,, M. and N. Zuber (1979), *Drag Coefficient and Relative Velocity in Bubbly Droplet or Particulate Flows*, AIChE Journal 25(5) p 843.

31. Ihme F., H. Schmidt-Traub, and H. Brauer (1972), Chemir-ING-Tech., **44(5)** pg. 306.

32. Ranz, W.E and W.R. Marshall Jr. (1952), *Evaporation From Drops*, Chemical Engineering Progress, 48(3) p141

33. Hughmark, G.A. (1967), *Mass and Heat Transfer from Rigid Spheres*, AIChE Journal, 13(6) p 1219

34. Hoffman, Joe D. (1992), *Numerical Methods for Engineers and Scientist*, McGraw-Hill, Inc., New York, New York.

35. Issa, R.I. (1985), *Solution of the Implicitly Discretised Fluid Flow Equations by Operator-Splitting*, Journal of Computational Physics, **62**, 40-65